

A MULTIREOLUTION SPACE-TIME ADAPTIVE SCHEME FOR THE BIDOMAIN MODEL IN ELECTROCARDIOLOGY

MOSTAFA BENDAHMANE^A, RAIMUND BÜRGER^A, AND RICARDO RUIZ BAIER^A

ABSTRACT. This work deals with the numerical solution of the monodomain and bidomain models of electrical activity of myocardial tissue. The bidomain model is a system consisting of a possibly degenerate parabolic PDE coupled with an elliptic PDE for the transmembrane and extracellular potentials, respectively. This system of two scalar PDEs is supplemented by a time-dependent ODE modeling the evolution of the so-called gating variable. In the simpler sub-case of the monodomain model, the elliptic PDE reduces to an algebraic equation. Two simple models for the membrane and ionic currents are considered, the Mitchell-Schaeffer model and the simpler FitzHugh-Nagumo model. Since typical solutions of the bidomain and monodomain models exhibit wavefronts with steep gradients, we propose a finite volume scheme enriched by a fully adaptive multiresolution method, whose basic purpose is to concentrate computational effort on zones of strong variation of the solution. Time adaptivity is achieved by two alternative devices, namely locally varying time stepping and a Runge-Kutta-Fehlberg-type adaptive time integration. A series of numerical examples demonstrates that these methods are efficient and sufficiently accurate to simulate the electrical activity in myocardial tissue with affordable effort. In addition, an optimal threshold for discarding non-significant information in the multiresolution representation of the solution is derived, and the numerical efficiency and accuracy of the method is measured in terms of CPU time speed-up, memory compression, and errors in different norms.

1. INTRODUCTION

1.1. Scope. The obvious difficulty of performing direct measurements in electrocardiology has motivated wide interest in the numerical simulation of cardiac models. In 1952, Hodgkin and Huxley [27] introduced the first mathematical model of wave propagation in squid nerve, which was modified later on to describe several phenomena in biology. This led to the first physiological model of cardiac tissue [33] and many others. Among these models, the *bidomain model*, firstly introduced by Tung [42], is one of the most accurate and complete models for the theoretical and numerical study of the electric activity in cardiac tissue. The bidomain equations result from the principle of conservation of current between the intra- and extracellular domains, followed by a homogenization process (see e.g. [3, 14, 28]) derived from a scaled version of a cellular model on a periodic structure of cardiac tissue. Mathematically, the bidomain model is a coupled system consisting of a scalar, possibly degenerate parabolic PDE coupled with a scalar elliptic PDE for the transmembrane potential and the extracellular potential, respectively. These equations are supplemented by a time-dependent ODE for the so-called gating variable, which is defined at every point of the spatial computational domain. Here, the term “bidomain” reflects that in general, the intra- and extracellular tissues have different longitudinal and transversal (with respect to the fiber) conductivities; if these are equal, then the model is termed *monodomain model*, and the elliptic PDE reduces to an algebraic equation. The degenerate structure of the mathematical formulation of the bidomain model is essentially due to the differences between the intra- and extracellular anisotropy of the cardiac tissue [3, 17].

The bidomain model represents a computational challenge since the width of an excitation front is roughly two orders of magnitude smaller than the long axis of a human-size right ventricle. This local feature, along

Date: February 10, 2022.

1991 Mathematics Subject Classification. 74S05, 65M99, 35K65.

Key words and phrases. Bidomain model, parabolic-elliptic system, fully adaptive multiresolution schemes, Runge-Kutta-Fehlberg, local time stepping, electrocardiology.

^ADepartamento de Ingeniería Matemática, Facultad de Ciencias Físicas y Matemáticas, Universidad de Concepción, Casilla 160-C, Concepción, Chile. E-mail: mostafab@ing-mat.udec.cl, rburger@ing-mat.udec.cl, rruiz@ing-mat.udec.cl.

with strongly varying time scales in the reaction terms, produces solutions with sharp propagating wave fronts in the potential field, which almost precludes simulations with uniform grids. Clearly, cardiac simulations should be based on space- (and also time-) adaptive methods.

It is the purpose of this paper to develop a fully adaptive multiresolution (MR) scheme with locally varying space-time stepping (LTS) and adaptive time step control by means of a Runge-Kutta-Fehlberg (RKF) method. These strategies are of different nature, but do not exclude each other; rather, they may be combined to obtain a potentially more powerful method (as is suggested e.g. in [21]; however, herein we do not pursue that approach). We furthermore address the deduction of an optimal threshold value for discarding non-significant data, which permits to achieve significant data compression. Previous experience with degenerate parabolic equations and reaction-diffusion systems [2, 7, 8, 9, 36, 37] suggests that the MR device should provide an efficient tool for solving the bidomain equations, and in this same spirit, we construct the corresponding extension of the MR method with the novel application to the bidomain and monodomain models in mind.

The efficiency of the MR method is a consequence of the fact that at each time step, the solution is encoded with respect to a MR basis corresponding to a hierarchy of nested grids. The size of the details determines the level of refinement needed to obtain an accurate local representation of the solution. Therefore, an adaptive mesh is evolved in time by refining and coarsening in a suitable way, by means of a strategy based on the prediction of the displacement and creation of singularities in the solution.

We apply the MR approach to an explicit finite volume (FV) method in each time step. Since the computational effort required for integrating a system of equations for one time step is usually substantially higher for an implicit scheme when compared to explicit schemes, implicit schemes may be less efficient than explicit ones, especially when the overall number of time steps is large (see e.g. [11]).

1.2. Related work. To further put this work into the proper perspective, we first mention that standard theory for coupled parabolic-elliptic systems (see e.g. [10]) does not apply naturally to the bidomain equations, since the anisotropies of the intra- and extracellular media differ and the resulting system is of degenerate parabolic type. Colli Franzone and Savaré [17] present a weak formulation for the bidomain model and show that it has a structure suitable for applying the theory of evolution variational inequalities in Hilbert spaces. Bendahmane and Karlsen [3] prove existence and uniqueness for the bidomain equations using the Faedo-Galerkin method and compactness theory for the existence part, and Bourgault et al. [6] prove existence and uniqueness for the bidomain equations by first reformulating the problem as a single parabolic PDE, and then applying a semigroup approach.

From a computational point of view, substantial contributions have been made in adaptivity for cardiac models. However, the approach presented herein differs to the best of our knowledge from other adaptive approaches in the literature. These alternative techniques include adaptive mesh refinement (AMR) (e.g., [11, 41]), adaptive finite element methods using a posteriori error techniques (see, e.g., [14]) or multigrid methods applied to finite elements. Furthermore, Quan et al. [35] present a domain decomposition approach using an alternating direction implicit (ADI) method. With respect to time adaptivity, Skouibine et al. [39] present a predictor-corrector time stepping strategy to accelerate a given finite differences scheme for the bidomain equations using active membrane kinetics (Luo-Rudy phase II). Cherry et al. [11] use local time stepping, similar to the method introduced in the germinal work of Berger and Oliger [5], to accelerate a reference scheme. Parallelized versions of part of the methods mentioned above are presented, for example, by Colli Franzone and Pavarino [15] and Saleheen and Ng [38].

MR schemes for hyperbolic partial differential equations were first proposed by Harten [26]. We refer to the work of Müller [30] for a survey on MR methods, see also Chiavassa et al. [12]. As stated above, the idea behind the MR method is to accelerate a reference discretization scheme while controlling the error. In the context of fully adaptive MR methods [13], the mathematical analysis is complete only in the case of a scalar conservation law, but in practice, these techniques have been used by several groups (see e.g. [2, 21, 30, 31, 37]) to successfully solve a wide class of problems, including applications to multidimensional systems. For more details on the framework of classical MR methods for hyperbolic partial differential equations, we also refer to Cohen et al. [13] and Dahmen et al. [19].

1.3. Outline of the paper. The remainder of this paper is organized as follows. In Section 2, the bidomain and monodomain models of cardiac tissue are introduced. The general bidomain model can be expressed as a coupled system of a parabolic PDE and an elliptic PDE plus an ODE for the evolution of the local gating variable, while the monodomain model, which arises as a particular sub-case of the bidomain model, is defined by a reaction-diffusion equation, which is again supplemented with an ODE for the gating variable. Section 3 deals with the construction of an appropriate FV method for the solution of both the parabolic-elliptic system and the reaction-diffusion equation arising from the bidomain and monodomain models, respectively. Next, in Section 4 we develop the MR analysis used to endow the reference finite FV schemes with space adaptivity. More precisely, in Section 4.1 we introduce the wavelet basis underlying the multiresolution representation with the pertinent projection operator. In Section 4.2, the prediction operator and the detail coefficients are introduced. Small detail coefficients on fine levels of resolution may be discarded (this operation is called thresholding), which allows for substantial data compression. In Section 4.3, we recall the graded tree data structure used for storage of the numerical solution, and which is introduced for ease of navigation. In Section 4.4 we outline an error analysis, similar to that conducted in [8, 9, 37] and motivated by the rigorous analysis of Cohen et al. [13], which justifies the choice of a reference tolerance ε_R . In turn, this quantity determines the comparison values ε_l used for the thresholding operation at each level l of multiresolution. The basic goal is to choose the threshold values in such a way that the resulting multiresolution scheme has the same order of accuracy as the usual finite volume scheme.

In Section 5 we address two strategies for the adaptive evolution in time of the space-adaptive MR scheme, namely the locally varying time stepping (LTS, Section 5.1) and a variant of the well-known Runge-Kutta-Fehlberg (RKF, Section 5.2) method. Finally, in Section 6 we present numerical examples putting into evidence the efficiency of the underlying methods. Some conclusions that can be drawn from the paper about the effectiveness of our methods and statement of possible further extensions to our research are given in Section 7, and in the Appendix we present a brief description of the LTS and general MR algorithms.

2. THE MACROSCOPIC BIDOMAIN AND MONODOMAIN MODELS

The spatial domain for our models is a bounded open subset $\Omega \subset \mathbb{R}^2$ with a piecewise smooth boundary $\partial\Omega$. This represents a two-dimensional slice of the cardiac muscle regarded as two interpenetrating and superimposed (anisotropic) continuous media, namely the intracellular (i) and extracellular (e) tissues. These tissues occupy the same two-dimensional area, and are separated from each other (and connected at each point) by the cardiac cellular membrane. The quantities of interest are *intracellular* and *extracellular* electric potentials, $u_i = u_i(x, t)$ and $u_e = u_e(x, t)$, at $(x, t) \in \Omega_T := \Omega \times (0, T)$. Their difference $v = v(x, t) := u_i - u_e$ is known as the *transmembrane potential*. The conductivity of the tissue is represented by scaled tensors $\mathbf{M}_i(x)$ and $\mathbf{M}_e(x)$ given by

$$\mathbf{M}_j(x) = \sigma_j^t \mathbf{I} + (\sigma_j^l - \sigma_j^t) \mathbf{a}_l(x) \mathbf{a}_l^T(x),$$

where $\sigma_j^l = \sigma_j^l(x) \in C^1(\mathbb{R}^2)$ and $\sigma_j^t = \sigma_j^t(x) \in C^1(\mathbb{R}^2)$, $j \in \{e, i\}$, are the intra- and extracellular conductivities along and transversal to the direction of the fiber (parallel to $\mathbf{a}_l(x)$), respectively.

For fibers aligned with the axis, $\mathbf{M}_i(x)$ and $\mathbf{M}_e(x)$ are diagonal matrices: $\mathbf{M}_i(x) = \text{diag}(\sigma_i^l, \sigma_i^t)$ and $\mathbf{M}_e(x) = \text{diag}(\sigma_e^l, \sigma_e^t)$. When the so-called *anisotropy ratios* σ_i^l/σ_i^t and σ_e^l/σ_e^t are equal, we are in the case of *equal anisotropy*, but generally the conductivities in the longitudinal direction l are higher than those across the fiber (direction t); such a case is called *strong anisotropy* of electrical conductivity. When the fibers rotate from bottom to top, this type of anisotropy is often referred to as *rotational anisotropy*.

The bidomain model is given by the following coupled reaction-diffusion system [40, 43]:

$$\begin{aligned} \beta c_m \partial_t v - \nabla \cdot (\mathbf{M}_i(x) \nabla u_i) + \beta I_{\text{ion}}(v, w) &= 0, \\ \beta c_m \partial_t v + \nabla \cdot (\mathbf{M}_e(x) \nabla u_e) + \beta I_{\text{ion}}(v, w) &= I_{\text{app}}, \\ \partial_t w - H(v, w) &= 0, \end{aligned} \quad (x, t) \in \Omega_T. \quad (2.1)$$

Here, $c_m > 0$ is the so-called *surface capacitance* of the membrane, β is the surface-to-volume ratio, and $w(x, t)$ is the so-called *gating* or *recovery variable*, which also takes into account the concentration variables. The stimulation currents applied to the extracellular space are represented by the function $I_{\text{app}} = I_{\text{app}}(x, t)$.

The functions $H(v, w)$ and $I_{\text{ion}}(v, w)$ correspond to the fairly simple Mitchell-Schaeffer membrane model [29] for the membrane and ionic currents:

$$H(v, w) = \frac{w_{\infty}(v/v_p) - w}{R_m c_m \eta_{\infty}(v/v_p)}, \quad I_{\text{ion}}(v, w) = \frac{v_p}{R_m} \left(\frac{v}{v_p \eta_2} - \frac{v^2(1 - v/v_p)w}{v_p^2 \eta_1} \right), \quad (2.2)$$

where the dimensionless functions $\eta_{\infty}(s)$ and $w_{\infty}(s)$ are given by $\eta_{\infty}(s) = \eta_3 + (\eta_4 - \eta_3)\mathcal{H}(s - \eta_5)$ and $w_{\infty}(s) = \mathcal{H}(s - \eta_5)$, where \mathcal{H} denotes the Heaviside function, R_m is the surface resistivity of the membrane, and v_p and η_1, \dots, η_5 are given parameters. A simpler choice for the membrane kinetics is the widely known FitzHugh-Nagumo model [25, 32], which is often used to avoid computational difficulties arising from a large number of coupling variables. This model is specified by

$$H(v, w) = av - bw, \quad I_{\text{ion}}(v, w) = -\lambda(w - v(1 - v)(v - \theta)), \quad (2.3)$$

where a, b, λ and θ are given parameters.

We rewrite (2.1) equivalently in terms of v and u_e as the strongly coupled parabolic-elliptic PDE-ODE system (see e.g. [40, 43]):

$$\beta c_m \partial_t v + \nabla \cdot (\mathbf{M}_e(x) \nabla u_e) + \beta I_{\text{ion}}(v, w) = I_{\text{app}}, \quad (2.4a)$$

$$\nabla \cdot ((\mathbf{M}_i(x) + \mathbf{M}_e(x)) \nabla u_e) + \nabla \cdot (\mathbf{M}_i(x) \nabla v) = I_{\text{app}}, \quad (2.4b)$$

$$\partial_t w - H(v, w) = 0, \quad (x, t) \in \Omega_T. \quad (2.4c)$$

We utilize zero flux boundary conditions, representing an isolated piece of cardiac tissue:

$$(\mathbf{M}_j(x) \nabla u_j) \cdot \mathbf{n} = 0 \text{ on } \Sigma_T := \partial\Omega \times (0, T), \quad j \in \{e, i\}, \quad (2.5)$$

and impose initial conditions (which are degenerate for the transmembrane potential v):

$$v(0, x) = v_0(x), \quad w(0, x) = w_0(x), \quad x \in \Omega. \quad (2.6)$$

For the solution v of the bidomain model, we require the initial datum v_0 to be compatible with (2.5). Therefore, if we fix both $u_j(0, x)$, $j \in \{e, i\}$ as initial data, the problem may become unsolvable, since the time derivative involves only $v = u_i - u_e$ (this is also referred as *degeneracy in time*). Thus, we impose the compatibility condition

$$\int_{\Omega} u_e(x, t) dx = 0 \quad \text{for a.e. } t \in (0, T). \quad (2.7)$$

In the case that $\mathbf{M}_i \equiv \lambda \mathbf{M}_e$ for some constant $\lambda \in \mathbb{R}$, the system (2.1) is equivalent to a scalar parabolic equation for the transmembrane potential v , coupled to an ODE for the gating variable w . This parabolic equation is obtained by multiplying the first equation in (2.1) by $1/(1 + \lambda)$, the second by $\lambda/(1 + \lambda)$ and adding the resulting equations. The final *monodomain model* can be stated as follows:

$$\beta c_m \partial_t v - \nabla \cdot \left(\frac{\mathbf{M}_i}{1 + \lambda} \nabla v \right) + \beta I_{\text{ion}}(v, w) = \frac{\lambda}{1 + \lambda} I_{\text{app}}, \quad (2.8)$$

$$\partial_t w - H(v, w) = 0, \quad (x, t) \in \Omega_T.$$

This model is, of course, significantly less involved and requires substantially less computational effort than the bidomain model, and even though the assumption of equal anisotropy ratios is very strong and generally unrealistic, the monodomain model is adequate for a qualitative investigation of repolarization sequences and the distribution of patterns of durations of the action potential [16].

We assume that the functions \mathbf{M}_j , $j \in \{e, i\}$, I_{ion} , and H are sufficiently smooth so that the following definitions of weak solutions make sense. Furthermore, we assume that $I_{\text{app}} \in L^2(\Omega_T)$ and $\mathbf{M}_j \in L^\infty(\Omega)$ and $\mathbf{M}_j \boldsymbol{\xi} \cdot \boldsymbol{\xi} \geq C_M |\boldsymbol{\xi}|^2$ for a.e. $x \in \Omega$, for all $\boldsymbol{\xi} \in \mathbb{R}^2$, $j \in \{e, i\}$, and a constant $C_M > 0$. For later reference, we now state the definitions of a weak solution for the bidomain and the monodomain model, respectively.

Definition 2.1. A triple $\mathbf{u} = (v, u_e, w)$ of functions is a weak solution of the bidomain model (2.4)–(2.6) if $v, u_e \in L^2(0, T; H^1(\Omega))$, $w \in C([0, T], L^2(\Omega))$, (2.7) is satisfied, and the following identities hold for all test

functions $\varphi, \psi, \xi \in \mathcal{D}([0, T) \times \bar{\Omega})$:

$$\begin{aligned} \beta c_m \int_{\Omega} v_0(x) \varphi(0, x) dx + \iint_{\Omega_T} \left\{ \beta c_m v \partial_t \varphi - \mathbf{M}_e(x) \nabla u_e \cdot \nabla \varphi + \beta I_{\text{ion}} \varphi \right\} dx dt &= \iint_{\Omega_T} I_{\text{app}} \varphi dx dt, \\ \iint_{\Omega_T} \left\{ -(\mathbf{M}_i(x) + \mathbf{M}_e(x)) \nabla u_e \cdot \nabla \psi - \mathbf{M}_i(x) \nabla v \cdot \nabla \psi \right\} dx dt &= \iint_{\Omega_T} I_{\text{app}} \varphi dx dt, \\ - \int_{\Omega} w_0(x) \xi(0, x) dx - \iint_{\Omega_T} w \partial_t \xi dx dt &= \iint_{\Omega_T} H \xi dx dt. \end{aligned}$$

Definition 2.2. A pair $\mathbf{u} = (v, w)$ of functions is a weak solution of the monodomain model (2.8) if $v \in L^2(0, T; H^1(\Omega))$, $w \in C([0, T], L^2(\Omega))$, and the following identities hold for all test functions $\varphi, \xi \in \mathcal{D}([0, T) \times \bar{\Omega})$:

$$\begin{aligned} &\beta c_m \int_{\Omega} v_0(x) \varphi(0, x) dx \\ &+ \iint_{\Omega_T} \left\{ \beta c_m v \partial_t \varphi + \beta I_{\text{ion}} \varphi - \frac{1}{1 + \lambda} \mathbf{M}_i \nabla v \cdot \nabla \varphi \right\} dx dt = \frac{\lambda}{1 + \lambda} \iint_{\Omega_T} I_{\text{app}} \varphi dx dt, \\ &- \int_{\Omega} w_0(x) \xi(0, x) dx - \iint_{\Omega_T} w \partial_t \xi dx dt = \iint_{\Omega_T} H \xi dx dt. \end{aligned}$$

3. THE REFERENCE FINITE VOLUME SCHEME

To define the FV scheme for approximating solutions to the bidomain equations (2.4), we follow the framework of [23]. An admissible mesh for Ω is formed by a family \mathcal{T} of control volumes (open and convex polygons) of maximum diameter h . (From the next section on, we will use only Cartesian meshes, however the following description is in a more general setting.) For all $K \in \mathcal{T}$, x_K denotes the center of K , $N(K)$ is the set of neighbors of K , $\mathcal{E}_{\text{int}}(K)$ is the set of edges of K in the interior of \mathcal{T} , and $\mathcal{E}_{\text{ext}}(K)$ the set of edges of K on the boundary $\partial\Omega$. For all $L \in N(K)$, $d(K, L)$ denotes the distance between x_K and x_L , $\sigma_{K,L}$ is the interface between K and L , and $\eta_{K,L}$ ($\eta_{K,\sigma}$, respectively) is the unit normal vector to $\sigma_{K,L}$ ($\sigma \in \mathcal{E}_{\text{ext}}(K)$, respectively) oriented from K to L (from K to $\partial\Omega$, respectively). For all $K \in \mathcal{T}$, $|K|$ stands for the measure of the cell K . The admissibility of \mathcal{T} implies that $\bar{\Omega} = \cup_{K \in \mathcal{T}} \bar{K}$, $K \cap L = \emptyset$ if $K, L \in \mathcal{T}$ and $K \neq L$, and there exist a finite sequence $(x_K)_{K \in \mathcal{T}}$ for which $\overline{x_K x_L}$ is orthogonal to $\sigma_{K,L}$.

Now, consider $K \in \mathcal{T}$ and $L \in N(K)$ with common vertices $(a_{\ell,K,L})_{1 \leq \ell \leq I}$ with $I \in \mathbb{N} \setminus \{0\}$ and let $T_{K,L}$ ($T_{K,\sigma}^{\text{ext}}$ for $\sigma \in \mathcal{E}_{\text{ext}}(K)$, respectively) be the open and convex polygon with vertices (x_K, x_L) (x_K , respectively) and $(a_{\ell,K,L})_{1 \leq \ell \leq I}$. Notice that Ω can be decomposed into $\bar{\Omega} = \cup_{K \in \mathcal{T}} ((\cup_{L \in N(K)} \bar{T}_{K,L}) \cup (\cup_{\sigma \in \mathcal{E}_{\text{ext}}(K)} \bar{T}_{K,\sigma}^{\text{ext}}))$.

For all $K \in \mathcal{T}$, the approximation $\nabla_h u_h$ of ∇u is defined by

$$\nabla_h u_h(x) := \begin{cases} \frac{|\sigma_{K,L}|}{|T_{K,L}|} (u_L - u_K) \eta_{K,L} & \text{if } x \in T_{K,L}, \\ 0 & \text{if } x \in T_{K,\sigma}^{\text{ext}}. \end{cases}$$

To discretize (2.4)–(2.6), we choose an admissible discretization of Q_T , consisting of an admissible mesh of Ω and a time step size $\Delta t > 0$. For example, we could choose $N > 0$ as the smallest integer such that $N\Delta t \geq T$, and set $t^n := n\Delta t$ for $n \in \{0, \dots, N\}$. However, for reasons stated further below, we assume that the time step size Δt is determined anew for each iteration, and present the scheme as it applies to advance the solution from t^n to $t^{n+1} := t^n + \Delta t$.

On each cell $K \in \mathcal{T}$, (positive definite) conductivity tensors are defined by

$$\mathbf{M}_{j,K} = \frac{1}{|K|} \int_{\Omega} \mathbf{M}_j(x) dx, \quad j \in \{e, i\}.$$

Let $F_{j,K,L}$ be an approximation of

$$\int_{\sigma_{K,L}} \mathbf{M}_j(x) \nabla u_j \cdot \eta_{K,L} d\gamma$$

for $j \in \{e, i\}$, and for $K \in \mathcal{T}$ and $L \in N(K)$, let

$$M_{j,K,L} = \left| \frac{1}{|K|} \int_K \mathbf{M}_j(x) dx \eta_{K,L} \right| := |\mathbf{M}_{j,K} \eta_{K,L}|, \quad j \in \{e, i\}.$$

Here $|\cdot|$ stands for the Euclidean norm. The diffusive fluxes $\mathbf{M}_j(x) \nabla u_j \cdot \eta_{K,L}$ on $\sigma_{K,L}$ are approximated by

$$\begin{aligned} & \int_{\sigma_{K,L}} (\mathbf{M}_j(x) \nabla u_j) \cdot \eta_{K,L} d\gamma \\ & \approx |\sigma_{K,L}| \nabla u_j(y_\sigma) \cdot (\mathbf{M}_{j,K} \eta_{K,L}) = |\sigma_{K,L}| M_{j,K,L} \nabla u_j(y_\sigma) \cdot \frac{y_\sigma - x_K}{d(K, \sigma_{K,L})} \approx |\sigma_{K,L}| M_{j,K,L} \frac{u_{j,\sigma} - u_{j,K}}{d(K, \sigma_{K,L})}, \end{aligned}$$

where y_σ is the center of $\sigma_{K,L}$ and $u_{j,\sigma}$ is an approximation of $u_j(y_\sigma)$, $j \in \{e, i\}$. The resulting approximation of fluxes is consistent [23]. In addition, the scheme should be conservative. This property enables us to determine the additional unknowns $u_{j,\sigma}$, and to compute the numerical fluxes on internal edges:

$$F_{j,K,L} = d_{j,K,L}^* \frac{|\sigma_{K,L}|}{d(K, L)} (u_{j,L} - u_{j,K}) \quad \text{if } L \in N(K), \quad (3.1)$$

where we define

$$d_{j,K,L}^* := \frac{M_{j,K,L} M_{j,L,K}}{d(K, \sigma_{K,L}) M_{j,K,L} + d(L, \sigma_{K,L}) M_{j,L,K}} d(K, L),$$

while we discretize the zero-flux boundary condition by setting

$$F_{j,K,\sigma} = 0 \quad (3.2)$$

on boundary edges. Here, $d(K, \sigma_{K,L})$ and $d(L, \sigma_{K,L})$ are the distances from x_K and x_L to $\sigma_{K,L}$, respectively. We define cell averages of the unknowns $H(v, w)$ and $I_{\text{ion}}(v, w)$:

$$H_K^{n+1} := \frac{1}{\Delta t |K|} \int_{t^n}^{t^{n+1}} \int_K H(v(x, t), w(x, t)) dx dt, \quad I_{\text{ion},K}^{n+1} := \frac{1}{\Delta t |K|} \int_{t^n}^{t^{n+1}} \int_K I_{\text{ion}}(v(x, t), w(x, t)) dx dt,$$

and of the given function I_{app} :

$$I_{\text{app},K}^{n+1} := \frac{1}{\Delta t |K|} \int_{t^n}^{t^{n+1}} \int_K I_{\text{app}}(x, t) dx dt.$$

The computation starts from the initial cell averages

$$v_K^0 = \frac{1}{|K|} \int_K v_0(x) dx, \quad w_K^0 = \frac{1}{|K|} \int_K w_0(x) dx. \quad (3.3)$$

We now describe the finite volume scheme employed to advance the numerical solution from t^n to t^{n+1} , which is based on a simple explicit Euler time discretization. Assuming that at $t = t^n$, the quantities $u_{j,K}^n$, $j \in \{e, i\}$, $v_K^n = (u_{i,K}^n - u_{e,K}^n)$, and w_K^n are known for all $K \in \mathcal{T}$, we compute the values of these cell averages $u_{j,K}^{n+1}$, $j \in \{e, i\}$, $v_K^{n+1} = (u_{i,K}^{n+1} - u_{e,K}^{n+1})$ and w_K^{n+1} at $t = t^{n+1}$ from

$$\beta c_m |K| \frac{v_K^{n+1} - v_K^n}{\Delta t} + \sum_{L \in N(K)} d_{e,K,L}^* \frac{|\sigma_{K,L}|}{d(K, L)} (u_{e,L}^n - u_{e,K}^n) + \beta |K| I_{\text{ion},K}^n = |K| I_{\text{app},K}^n, \quad (3.4)$$

$$\sum_{L \in N(K)} \frac{|\sigma_{K,L}|}{d(K, L)} \left\{ (d_{i,K,L}^* + d_{e,K,L}^*) (u_{e,L}^{n+1} - u_{e,K}^{n+1}) + d_{i,K,L}^* (v_L^{n+1} - v_K^{n+1}) \right\} = |K| I_{\text{app},K}^n, \quad (3.5)$$

$$|K| \frac{w_K^{n+1} - w_K^n}{\Delta t} - |K| H_K^n = 0. \quad (3.6)$$

The order in which these equations are used to advance is explicitly stated in Algorithm 1 in Section 6.

The boundary condition (2.5) is taken into account by imposing zero fluxes on the external edges as in (3.2):

$$d_{j,K,\sigma}^* \frac{|\sigma_{K,L}|}{d(K, L)} (u_{j,L}^n - u_{j,K}^n) = 0 \quad \text{for } \sigma \in \mathcal{E}_{\text{ext}}(K), \quad j \in \{e, i\}, \quad n = 0, 1, 2, \dots \quad (3.7)$$

and the compatibility condition (2.7) is discretized via

$$\sum_{K \in \mathcal{T}} |K| u_{e,K}^n = 0, \quad n = 0, 1, 2, \dots$$

Analogously, a FV method for the monodomain model (2.8) is given by determining vectors v_K^{n+1} and w_K^{n+1} for $K \in \mathcal{T}$ and $n = 0, 1, 2, \dots$ such that for all $K \in \mathcal{T}$, we start from the initial data given by (3.3), and use the following formulas to advance the solution over one time step:

$$\begin{aligned} \beta c_m |K| \frac{v_K^{n+1} - v_K^n}{\Delta t} + \sum_{L \in N(K)} \frac{1}{1 + \lambda} d_{i,K,L}^* \frac{|\sigma_{K,L}|}{d(K,L)} (v_L^n - v_K^n) + \beta |K| I_{\text{ion},K}^n &= \frac{\lambda}{1 + \lambda} |K| I_{\text{app},K}^n, \\ |K| \frac{w_K^{n+1} - w_K^n}{\Delta t} - |K| H_K^{n+1} &= 0. \end{aligned}$$

A FV method for a slightly different version of the bidomain equations is analyzed in [4]. In that paper, the authors prove existence and uniqueness of solutions to an implicit FV scheme, and provide convergence results. On the other hand, following [4, 18, 23], we prove in [1] existence and uniqueness of approximate solutions (that is, well-definedness of the scheme) for an implicit version of the scheme considered herein, and show that it converges to a weak solution in the sense of Definition 2.1, under a mild condition that limits the time step size Δt (a CFL-type condition is, however, not imposed in [1]). Moreover, as in [2], we may deduce that in the case of Cartesian meshes, the explicit version of the FV method utilized herein, (3.3)–(3.7), is stable under the CFL condition

$$\Delta t \leq h \left(2 \max_{K \in \mathcal{T}} (|I_{\text{ion},K}^n| + |I_{\text{app},K}^n|) + 4h^{-1} \max_{K \in \mathcal{T}} (|M_{i,K}| + |M_{e,K}|) \right)^{-1}. \quad (3.8)$$

Notice that the values of $I_{\text{ion},K}^n$ and $I_{\text{app},K}^n$ depend on time. However, while I_{app} is a given control function for our model and therefore $\max_{K \in \mathcal{T}} |I_{\text{app},K}^n|$ can be assumed to be bounded, the quantity $I_{\text{ion},K}^n$ is not bounded a priori for arbitrarily large times. Consequently, in our computations, we evaluate the right-hand side of (3.8) after each iteration at $t = t^n$, and use (3.8) to define the time step size Δt to advance the solution from t^n to $t^{n+1} = t^n + \Delta t$.

4. MULTIRESOLUTION AND WAVELETS

4.1. Wavelet basis. Consider a rectangle which after a change of variables can be regarded as $\Omega = [0, 1]^2$. We determine a nested mesh hierarchy $\Lambda_0 \subset \dots \subset \Lambda_L$, using an uniform dyadic partition of Ω . Here each grid $\Lambda_l := \{V_{(i,j),l}\}_{(i,j)}$, with (i, j) to be defined, is formed by the control volumes at each level $V_{(i,j),l} := 2^{-l} [i, i+1] \times [j, j+1]$, $i, j \in I_l = \{0, \dots, 2^l - 1\}$, $l = 0, \dots, L$. Here, $l = 0$ corresponds to the coarsest and $l = L$ to the finest level. The nestedness of the grid hierarchy is made precise by the refinement sets $\mathcal{M}_{(i,j),l} = \{2(i, j) + \mathbf{e}\}$, $\mathbf{e} \in E := \{0, 1\}^2$, which satisfy $\#\mathcal{M}_{(i,j),l} = 4$. For $x = (x_1, x_2) \in V_{(i,j),l}$ the *scale box function* is defined as

$$\tilde{\varphi}_{(i,j),l}(x) := \frac{1}{|V_{(i,j),l}|} \chi_{V_{(i,j),l}}(x) = 2^{2l} \chi_{[0,1]^2}(2^l x_1 - i, 2^l x_2 - j),$$

and the averages of any function $u(\cdot, t) \in L^1(\Omega)$ for the cell $V_{(i,j),l}$ may be expressed equivalently as the inner product $u_{(i,j),l} := \langle u, \tilde{\varphi}_{(i,j),l} \rangle_{L^1(\Omega)}$. We are now ready to define the following two-scale relation for cell averages and box functions:

$$\begin{aligned} \tilde{\varphi}_{(i,j),l} &= \sum_{\mathbf{r} \in \mathcal{M}_{(i,j),l}} \frac{|V_{\mathbf{r},l+1}|}{|V_{(i,j),l}|} \tilde{\varphi}_{\mathbf{r},l+1} = \frac{1}{4} \sum_{(p,q) \in E} \tilde{\varphi}_{(2i+p, 2j+q), l+1}, \\ \bar{u}_{(i,j),l} &= \sum_{\mathbf{r} \in \mathcal{M}_{(i,j),l}} \frac{|V_{\mathbf{r},l+1}|}{|V_{(i,j),l}|} u_{\mathbf{r},l+1} = \frac{1}{4} \sum_{(p,q) \in E} u_{(2i+p, 2j+q), l+1}, \end{aligned} \quad (4.1)$$

which defines a *projection* operator, which allows us to move from finer to coarser levels. For $x \in V_{2(i,j)+\mathbf{a},l+1}$ with $\mathbf{a} \in E$, we define the *wavelet function* depending on the box functions on a finer level

$$\tilde{\psi}_{(i,j),\mathbf{e},l} = \sum_{\mathbf{a} \in E} 2^{-2} (-1)^{\mathbf{a} \cdot \mathbf{e}} \tilde{\varphi}_{2(i,j)+\mathbf{a},l+1} = \sum_{\mathbf{r} \in \mathcal{M}_{(i,j),l}} \frac{|V_{\mathbf{r}=2(i,j)+\mathbf{a},l+1}|}{|V_{(i,j),l}|} (-1)^{\mathbf{a} \cdot \mathbf{e}} \tilde{\varphi}_{\mathbf{r},l+1}.$$

The number of related wavelets is $\#\mathcal{M}_{(i,j),l} - 1 = 3$. Since $\mathbf{r} \cdot \mathbf{e} \in \{0, 1, 2\}$ for $\mathbf{r}, \mathbf{e} \in E$, we have for instance that

$$\tilde{\psi}_{(i,j),(1,0),l} = \frac{1}{4} (\tilde{\varphi}_{2(i,j),l+1} + \tilde{\varphi}_{2(i,j)+(0,1),l+1} - \tilde{\varphi}_{2(i,j)+(1,0),l+1} - \tilde{\varphi}_{2(i,j)+(1,1),l+1}).$$

Doing this for all $\mathbf{e} \in E^* := E \setminus \{(0,0)\}$ yields an inverse two-scale relation (see [30]), namely

$$\tilde{\varphi}_{2(i,j)+\mathbf{a},l+1} = \sum_{\mathbf{e} \in E} (-1)^{\mathbf{a} \cdot \mathbf{e}} \tilde{\psi}_{(i,j),\mathbf{e},l}, \quad \mathbf{a} \in E.$$

This equation is related to the concept of *stable completions* [30]. Roughly speaking, the L^∞ -counterparts of the wavelet functions $\{\tilde{\psi}_{(i,j),l}\}_{i,j \in I_l}$ form a completion of the L^∞ -counterpart of the basis system $\{\tilde{\varphi}_{(i,j),l}\}_{i,j \in I_l}$, and this determines the existence of a biorthogonal system.

4.2. Detail coefficients. For $\mathbf{e} \in E^*$, we introduce the *details*, which will be crucial to detect zones with steep gradients: $d_{(i,j),\mathbf{e},l} := \langle u, \tilde{\psi}_{(i,j),\mathbf{e},l} \rangle$. These detail coefficients also satisfy a two-scale relation, namely

$$d_{(i,j),\mathbf{e},l} = \frac{1}{4} \sum_{2(i,j)+\mathbf{a} \in \mathcal{M}_{(i,j),l}} (-1)^{\mathbf{a} \cdot \mathbf{e}} u_{2(i,j)+\mathbf{a},l+1}. \quad (4.2)$$

An appealing feature is that we can determine a transformation between the cell averages on level L and the cell averages on level 0 plus a series of details. This can be achieved by applying recursively the two-scale relations (4.1) and (4.2); but we also require this transformation to be reversible:

$$\tilde{u}_{(i,j),l+1} = \sum_{\mathbf{r} \in \tilde{S}_{(i,j)}^l} g_{(i,j),\mathbf{r}}^l u_{\mathbf{r},l}, \quad \tilde{S}_{(i,j)}^l := \{V_{([i/2]+r_1, [j/2]+r_2),l}\}_{r_1, r_2 \in \{-s, \dots, 0, \dots, s\}}, \quad (4.3)$$

where $\tilde{S}_{(i,j)}^l$ is the stencil of interpolation or *coarsening set*, $g_{(i,j),\mathbf{r}}^l$ are coefficients, and the tilde over u in the left-hand side of (4.3) means that this corresponds to a predicted value.

Relation (4.3) defines the so-called *prediction* operator, which allows us to move from coarser to finer resolution levels. In contrast to the projection, the prediction operator is not unique, but we will impose two constraints: to be consistent with the projection, in the sense that the prediction operator is the *right inverse* of the projection operator, and to be local, in the sense that the predicted value depends only on $\tilde{S}_{(i,j)}^l$. For sake of notation, in our case we may write (4.3) as

$$\tilde{u}_{(2i+e_1, 2j+e_2),l+1} = u_{(i,j),l} - (-1)^{e_1} Q_x - (-1)^{e_2} Q_y + (-1)^{e_1 e_2} Q_{xy},$$

where $e_1, e_2 \in \{0, 1\}$ and

$$\begin{aligned} Q_x &:= \sum_{n=1}^s \tilde{\gamma}_n (u_{(i+n,j),l} - u_{(i-n,j),l}), & Q_y &:= \sum_{p=1}^s \tilde{\gamma}_p (u_{(i,j+p),l} - u_{(i,j-p),l}), \\ Q_{xy} &:= \sum_{n=1}^s \tilde{\gamma}_n \sum_{p=1}^s \tilde{\gamma}_p (u_{(i+n,j+p),l} - u_{(i+n,j-p),l} - u_{(i-n,j+p),l} + u_{(i-n,j-p),l}). \end{aligned}$$

Here the corresponding coefficients are $\tilde{\gamma}_1 = -\frac{22}{128}$ and $\tilde{\gamma}_2 = \frac{3}{128}$ (see [37]).

From [19] we know that details are related to the regularity of a given function: if u is sufficiently smooth, then its detail coefficients decrease when going from coarser to finer levels:

$$|d_{(i,j),l}^u| \leq C 2^{-2lr} \|\nabla^{(r)} u\|_{L^\infty(V_{(i,j),l})},$$

where $r = 2s + 1$ is the number of vanishing moments of the wavelets. This means that the more regular u is over $V_{(i,j),l}$, the smaller is the corresponding detail coefficient. In view of this property, it is natural to attain data compression by discarding the information corresponding to small details. This is called *thresholding*.

Basically, we discard all the elements corresponding to details that are smaller in absolute value than a level-dependent tolerance ε_l ,

$$|d_{(i,j),l}^u| < \varepsilon_l.$$

Given a reference tolerance ε_R , which is determined by means of an error analysis (see Section 4.4), we determine ε_l by

$$\varepsilon_l = 2^{2(l-L)} \varepsilon_R. \quad (4.4)$$

4.3. Graded tree data structure. We organize the cell averages and corresponding details at different levels in a *dynamic graded tree*: whenever an element is included in the tree, all other elements corresponding to the same spatial region in coarser resolution levels are also included, and neighboring cells will differ by at most one refinement level. This choice guarantees the stability of the multiscale operations [13]. We denote by *root* the basis and by *node* an element of the tree. In two space dimensions, a parent node has four sons, and the sons of the same parent are called *brothers*. A node without sons is called a *leaf*. A given node has $s' = 2$ nearest neighbors in each spatial direction, called *nearest cousins*, needed for the computation of the fluxes of leaves; if these nearest cousins do not exist, we create them as *virtual leaves*. The leaves of the tree are the control volumes forming the adaptive mesh. We denote by Λ the set of all nodes of the tree and by $\mathcal{L}(\Lambda)$ the restriction of Λ to the leaves. We apply this MR representation to the spatial part of the function $\mathbf{u} = (v, u_e, w)$, which corresponds to the numerical solution of the underlying problem for each time step, so we need to update the tree structure for the proper representation of the solution during the evolution. To this end, we apply a thresholding strategy, but always keep the graded tree structure of the data. Once the thresholding is performed, we add to the tree a *safety zone*, so the new tree may contain the adaptive mesh for the next time step. The safety zone is generated by adding one finer level to the tree in all possible positions without violating the graded tree data structure. This device, first proposed by Harten [26], ensures that the graded tree adequately represents the solution in the next time step. Its effectiveness depends strongly on the assumption of finite propagation speed of the singularities.

Note that the fluxes are only computed at level $l + 1$ and we set the ingoing flux on the leaf at level l equal to the sum of the outgoing fluxes on the leaves of level $l + 1$ sharing the same edge

$$F_{(i+1,j),l \rightarrow (i,j),l} = F_{(2i+1,2j),l+1 \rightarrow (2i+2,2j),l+1} + F_{(2i+1,2j+1),l+1 \rightarrow (2i+2,2j+1),l+1}. \quad (4.5)$$

It is known that this choice decreases the number of costly flux evaluations without loosing the conservativity in the flux computation, and this represents a real advantage when using a graded tree structure, see e.g. [37] for more details. This advantage is lost for a non-graded tree structure, for which fluxes for leaves on an immediately finer level are not always available.

The *data compression rate* [8, 9] $\eta := \mathcal{N} / (2^{-(L+1)} \mathcal{N} + \#\mathcal{L}(\Lambda))$ is used to measure the improvement in data compression. Here, \mathcal{N} is the number of elements in the full finest grid at level L , and $\#\mathcal{L}(\Lambda)$ is the size of the set of leaves. We also measure the *speed-up* \mathcal{V} between the CPU time of the numerical solution obtained by the FV method and the CPU time of the numerical solution obtained by the MR method: $\mathcal{V} := \text{CPU time}_{\text{FV}} / \text{CPU time}_{\text{MR}}$.

4.4. Error analysis of the multiresolution scheme. Using the main properties of the reference FV scheme, such as the CFL stability condition and order of approximation in space, we can derive the optimal choice for the threshold parameter ε_R for the adaptive MR scheme. We can decompose the global error between the cell average values of the exact solution vector at the level L , denoted by $\mathbf{u}_{\text{ex}}^L = (v_{\text{ex}}^L, u_{e,\text{ex}}^L, w_{\text{ex}}^L)$, and those of the MR computation with a maximal level L , denoted by \mathbf{u}_{MR}^L , into two errors

$$\|\mathbf{u}_{\text{ex}}^L - \mathbf{u}_{\text{MR}}^L\| \leq \|\mathbf{u}_{\text{ex}}^L - \mathbf{u}_{\text{FV}}^L\| + \|\mathbf{u}_{\text{FV}}^L - \mathbf{u}_{\text{MR}}^L\|.$$

The first error on the right-hand side is called *discretization error* and the second *perturbation error*. Using this, the CFL condition (3.8), and the fact that $h = |\Omega|^{1/2} 2^{-L}$; we obtain that if the so-called *reference tolerance* for the numerical computations in Section 6 is set to

$$\varepsilon_R = C \frac{2^{-(\alpha+2)L}}{|\Omega| \max_{K \in \mathcal{T}} (|I_{\text{ion},K}| + 2|I_{\text{app},K}|) + |\Omega|^{3/2} 2^{2+L} \max_{K \in \mathcal{T}} (|M_{i,K}| + |M_{e,K}|)}, \quad (4.6)$$

then we can expect the discretization error and the perturbation error to be kept at the same order (see [8, 13, 37] for more details).

To measure errors between a reference solution u_{ex} and an approximate solution u_{MR} , we will use L^p -errors: $e_p = \|u_{\text{ex}}^n - u_{\text{MR}}^n\|_p$, $p = 1, 2, \infty$, where

$$e_\infty = \max_{(i,j,l) \in \mathcal{L}(\Lambda)} |u_{\text{ex},i,j,l}^n - u_{\text{MR},i,j,l}^n|; \quad e_p = \left(\frac{1}{|\mathcal{L}(\Lambda)|} \sum_{(i,j,l) \in \mathcal{L}(\Lambda)} |u_{\text{ex},i,j,l}^n - u_{\text{MR},i,j,l}^n|^p \right)^{1/p}, \quad p = 1, 2.$$

Here $u_{\text{ex},i,j,l}^n$ stands for the projection of the reference solution onto the leaf (i, j, l) .

5. TIME-STEP ACCELERATING METHODS

5.1. Local time stepping. We employ a version of the locally varying time stepping strategy introduced by Müller and Stiriba [31], and summarize here its principles. The basic idea is to enforce a local CFL condition by using the same CFL number for all scales, and evolving all leaves on level l using the local time step size

$$\Delta t_l = 2^{L-l} \Delta t, \quad l = L-1, \dots, 0,$$

where $\Delta t = \Delta t_L$ corresponds to the time step size on the finest level L . This strategy allows to increase the time step for the major part of the adaptive mesh without violating the CFL stability condition. The synchronization of the time stepping for the portions of the solution lying on different resolution levels will be automatically achieved after 2^l time steps using Δt_l . To additionally save computational effort, the tree is updated only each odd intermediate time step $1, 3, \dots, 2^L - 1$, and furthermore, the projection and prediction operators are performed only on scales occupied by the leaves of the current tree. For the rest of the intermediate time steps, we use the current (old) tree structure. For the sake of synchronization and conservativity of the flux computation, for coarse levels (scales without leaves), we use *the same* diffusive fluxes and sources computed in the previous intermediate time step, because the cell average on these scales are the same that in the previous intermediate time step. Only for scales containing leaves, we compute fluxes in the following way: if there is a leaf at the corresponding edge and at the same resolution level l , we simply perform a flux computation using the brother leaves, and the virtual leaves at the same level if necessary; and if there is a leaf at the corresponding cell edge but on a finer resolution level $l+1$ (*interface edge*), the flux will be determined as in (4.5), i.e., we compute the fluxes at a level $l+1$ on the same edge, and we set the ingoing flux on the corresponding edge at level l equal to the sum of the outgoing fluxes on the sons cells of level $l+1$ (for the same edge). To always have at hand the computed fluxes as in (4.5), we need to perform the locally varying time stepping recursively from fine to coarse levels.

5.2. A Runge-Kutta-Fehlberg method. In order to upgrade the FV scheme described in Section 3 to at least second order so that the second-order spatial accuracy is effective, we utilize an RKF method [24], which, apart from providing the necessary accuracy, also allows an adaptive control of the time step. For our models, we consider a vector-valued RKF method, i.e., $\mathbf{u} = (v, u_e, w)$ and its time-discretized form at step m , denoted by \mathbf{u}^m . For ease of discussion, we assume that the problem is written as $\partial_t \mathbf{u} = \mathcal{A}(t, \mathbf{u})$.

We use two Runge-Kutta methods, of orders $p = 3$ and $p - 1 = 2$

$$\hat{\mathbf{u}}^{m+1} = \mathbf{u}^m + \hat{b}_1 \bar{\kappa}_1 + \hat{b}_2 \bar{\kappa}_2 + \hat{b}_3 \bar{\kappa}_3, \quad \check{\mathbf{u}}^{m+1} = \mathbf{u}^m + \check{b}_1 \bar{\kappa}_1 + \check{b}_2 \bar{\kappa}_2 + \check{b}_3 \bar{\kappa}_3,$$

where

$$\begin{aligned} \bar{\kappa}_1 &:= \Delta t \mathcal{A}(t^m, \mathbf{u}^m), \\ \bar{\kappa}_2 &:= \Delta t \mathcal{A}(t^m + c_2 \Delta t, \mathbf{u}^m + a_{21} \bar{\kappa}_1), \\ \bar{\kappa}_3 &:= \Delta t \mathcal{A}(t^m + c_3 \Delta t, \mathbf{u}^m + a_{31} \bar{\kappa}_1 + a_{32} \bar{\kappa}_2), \end{aligned} \tag{5.1}$$

and the coefficients corresponding to the RK3(2) method are $c_2 = a_{21} = 1$, $c_3 = \frac{1}{2}$, $a_{31} = a_{32} = \frac{1}{4}$, $\hat{b}_1 = \hat{b}_2 = \frac{1}{6}$, $\hat{b}_3 = \frac{2}{3}$, $\check{b}_1 = \check{b}_2 = \frac{1}{2}$, and $\check{b}_3 = 0$. These values yield an optimal pair of embedded TVD-RK

Time	\mathcal{V}	η	L^1 -error	L^2 -error	L^∞ -error
$t = 0.0$ ms		170.22	4.31×10^{-4}	2.47×10^{-4}	3.99×10^{-4}
$t = 1.5$ ms	27.81	37.56	4.97×10^{-4}	1.96×10^{-4}	4.63×10^{-4}
$t = 3.5$ ms	26.47	29.89	5.23×10^{-4}	4.05×10^{-4}	4.82×10^{-4}
$t = 4.5$ ms	31.41	28.12	7.48×10^{-4}	4.29×10^{-4}	5.31×10^{-4}
$t = 5.5$ ms	30.62	24.70	1.04×10^{-3}	6.20×10^{-4}	6.79×10^{-4}

TABLE 1. Example 1 (Monodomain model): Corresponding simulated time, CPU ratio \mathcal{V} , compression rate η and normalized errors for v , using a MR method.

Time [ms]	\mathcal{V}	η	Potential	L^1 -error	L^2 -error	L^∞ -error
$t = 0.1$	13.74	19.39	v	3.68×10^{-4}	8.79×10^{-5}	6.51×10^{-4}
			u_e	2.01×10^{-4}	6.54×10^{-5}	5.22×10^{-4}
$t = 0.5$	21.40	17.63	v	4.06×10^{-4}	9.26×10^{-5}	6.83×10^{-4}
			u_e	2.79×10^{-4}	8.72×10^{-5}	5.49×10^{-4}
$t = 2.0$	25.23	17.74	v	4.37×10^{-4}	1.25×10^{-4}	6.88×10^{-4}
			u_e	3.48×10^{-4}	9.44×10^{-5}	6.11×10^{-4}
$t = 5.0$	26.09	16.35	v	5.29×10^{-4}	1.94×10^{-4}	7.20×10^{-4}
			u_e	4.15×10^{-4}	1.06×10^{-4}	6.32×10^{-4}

TABLE 2. Example 2 (bidomain model, one stimulus): Corresponding simulated time, CPU ratio \mathcal{V} , compression rate η and normalized errors.

methods of orders two and three. The truncation error between the two approximations for \mathbf{u}^{m+1} is estimated by

$$\bar{\delta}_{\text{old}} := \hat{\mathbf{u}}^{m+1} - \check{\mathbf{u}}^{m+1} = \sum_{i=1}^p (\hat{b}_i - \check{b}_i) \bar{\kappa}_i \sim (\Delta t)^p, \quad \delta_{\text{old}} := \|\bar{\delta}_{\text{old}}\|_\infty. \quad (5.2)$$

Then we can adjust the step size to achieve a prescribed accuracy δ_{desired} in time. The new time step is determined by $\Delta t_{\text{new}} = \Delta t_{\text{old}} |\delta_{\text{desired}} / \delta_{\text{old}}|^{1/p}$ with $p = 3$. To avoid excessively large time steps, we define a limiter function $\mathcal{S}(t) := (\mathcal{S}_0 - \mathcal{S}_{\min}) \exp(-t/\Delta t) + \mathcal{S}_{\min}$, where we choose $\mathcal{S}_0 = 0.1$ and $\mathcal{S}_{\min} = 0.01$. The new time step Δt_{new} is then defined as

$$\Delta t_{\text{new}} = \begin{cases} \Delta t_{\text{old}} |\delta_{\text{desired}} / \delta_{\text{old}}|^{1/p} & \text{if } |(\Delta t_{\text{new}} - \Delta t_{\text{old}}) / \Delta t_{\text{old}}| \leq \frac{1}{2} \mathcal{S}(t, \Delta t_{\text{old}}), \\ \frac{1}{2} \mathcal{S}(t, \Delta t_{\text{old}}) \Delta t_{\text{old}} + \Delta t_{\text{old}} & \text{otherwise.} \end{cases} \quad (5.3)$$

Notice that Δt_{new} is the time step size for computing \mathbf{u}^{m+2} . More details on the RKF scheme and its implementation can be found in [8, 20].

6. NUMERICAL EXAMPLES

We will present three test cases showing the efficiency of the previously described methods in capturing the dynamical evolution of electro-physiological waves for both the monodomain and bidomain models. Since we are dealing with multicomponent solutions, we emphasize that a single mesh is used to represent the vector of relevant variables. In the bidomain model, the anisotropies, mesh structures, and the size of the problem cause the sparse linear system corresponding to (3.5) to be ill-conditioned. This system needs to be solved in each time step, which is done by the Cholesky method. Before presenting the numerical results, we provide further details on the implementation of the numerical schemes.

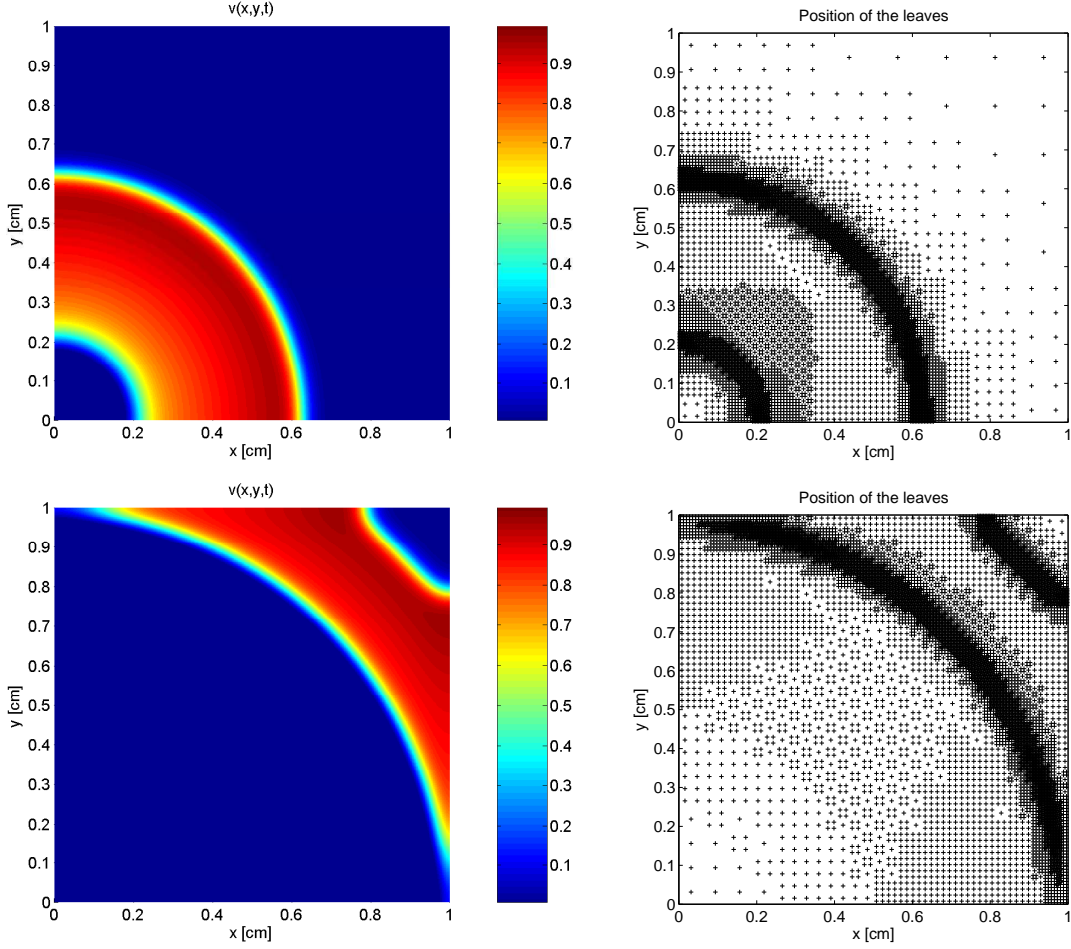


FIGURE 1. Example 1 (monodomain model): Numerical solution for v , measured in [mV] (left) and leaves of the corresponding tree at times (from top to bottom) $t = 1.5$ ms, $t = 3.5$ ms.

6.1. Implementation Issues. The following algorithm shows how the solution $\mathbf{u}^{n+1} = (v, u_e, w)^{n+1}$ is obtained in each time step

Algorithm 1 (General method).

- (1) Assume that u_i^n , u_e^n , v^n and w^n are known (at time t^n).
- (2) Solve the ODE

$$\partial_t w - H(v, w) = 0, \quad x \in \Omega,$$

approximately for $t^n < t \leq t^{n+1}$ with initial condition w^n and data v^n , i.e., compute w^{n+1} using (3.6).

- (3) Solve the parabolic PDE

$$\begin{aligned} \beta c_m \partial_t v + \nabla \cdot (\mathbf{M}_e(x) \nabla u_e) + \beta I_{\text{ion}}(v, w) &= I_{\text{app}}, \quad x \in \Omega, \\ (\mathbf{M}_e(x) \nabla u_e) \cdot \mathbf{n} &= 0 \quad \text{on } \partial\Omega \end{aligned}$$

approximately for $t^n < t \leq t^{n+1}$, with $v(t^n) = v^n$ and $w(t^n) = w^n$, i.e., calculate v^{n+1} using (3.4).

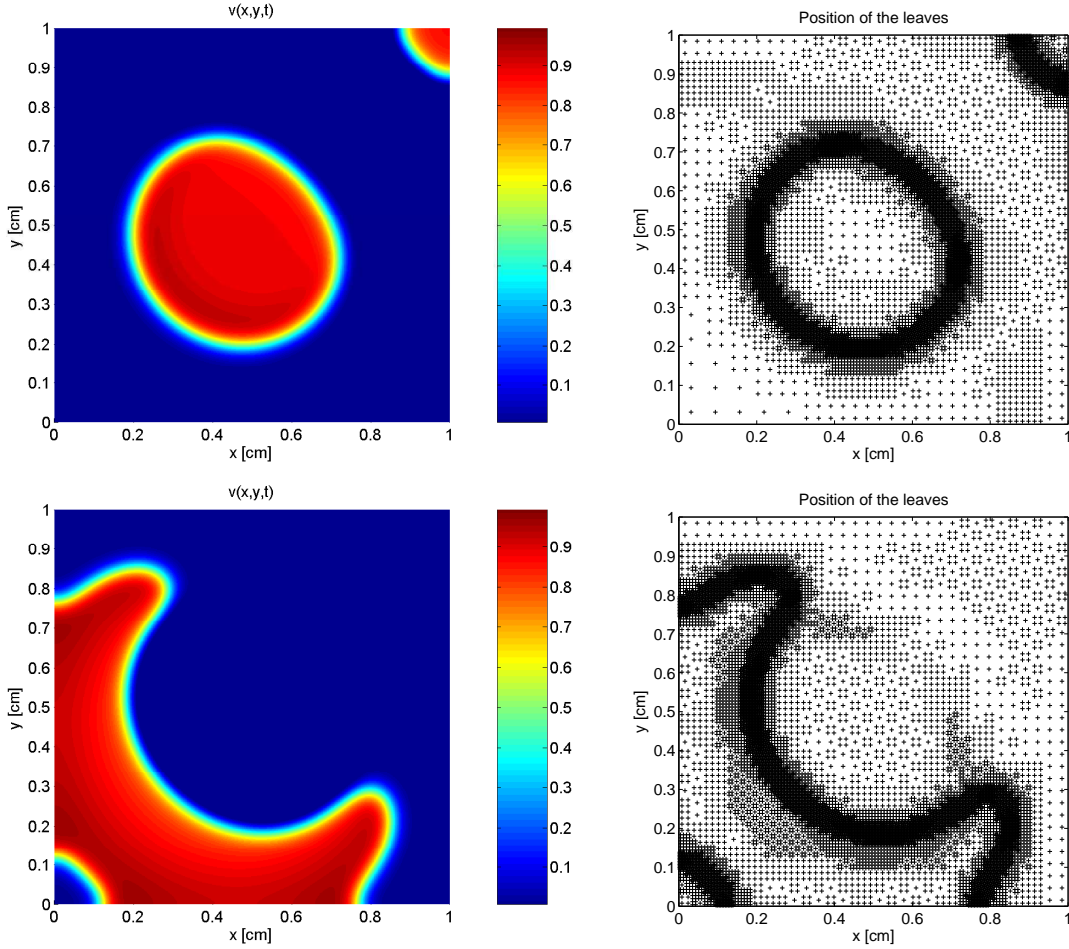


FIGURE 2. Example 1 (monodomain model): Numerical solution for v , measured in [mV] (left) and leaves of the corresponding tree at times (from top to bottom) $t = 4.5$ ms and $t = 5.5$ ms.

(4) *Solve the elliptic problem*

$$\begin{aligned} \nabla \cdot ((\mathbf{M}_i(x) + \mathbf{M}_e(x)) \nabla u_e) + \nabla \cdot (\mathbf{M}_i(x) \nabla v) &= I_{\text{app}}, \quad x \in \Omega \\ (\mathbf{M}_j(x) \nabla u_j) \cdot \mathbf{n} &= 0 \quad \text{on } \partial\Omega, j \in \{e, i\} \end{aligned}$$

approximately for $t^n < t \leq t^{n+1}$ with $v(t^n) = v^n$ and $u_e(t^n) = u_e^n$, i.e., determine u_e^{n+1} by solving the linear system (3.5).

This algorithm structure is usually preferred for systems involving parabolic and elliptic equation, since it explicitly isolates the solution of the elliptic problem from the rest of the computations [34].

For multicomponent solutions, there are many possible definitions for a scalar detail $d_{(i,j),l}$ that is calculated from the details of the components (see a brief discussion in [8]). To guarantee that the refinement and coarsening procedures are always on the safe side, in the sense that we always prefer to keep a position with a detail triple containing at least one component above the threshold (4.4), we will use $d_{(i,j),l}^u = \min\{d_{(i,j),l}^v, d_{(i,j),l}^{u_e}, d_{(i,j),l}^w\}$ and $d_{(i,j),l}^u = \max\{d_{(i,j),l}^v, d_{(i,j),l}^{u_e}, d_{(i,j),l}^w\}$ for the refinement and coarsening procedures, respectively. In practice, the details introduced in Section 4.2 are computed simply as the

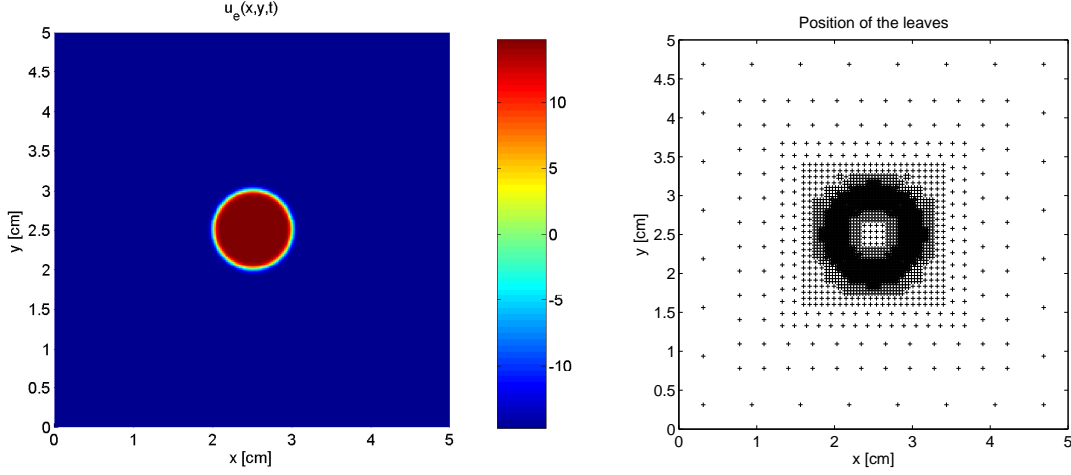


FIGURE 3. Example 2 (bidomain model, one stimulus): Initial condition for the extracellular potential u_e , and leaves of the corresponding tree data structure.

differences between the "exact" and the predicted value:

$$d_{(i,j),l}^{\mathbf{u}} := \mathbf{u}_{(i,j),l} - \hat{\mathbf{u}}_{(i,j),l}.$$

In (4.6) α stands for the accuracy order of the FV reference scheme, and numerical experience gives $\alpha = 1.09$. To choose an acceptable value for the factor C , a series of computations (not completely shown here) with different tolerances are needed in each case, prior to final computations. We basically choose the largest available candidate value for C such that the same order of accuracy as that of the reference FV scheme (same slope) is maintained and the data compression rate η and the speed-up \mathcal{V} are maximized (see Figure 6). In [2] we give a detailed description of the multiresolution algorithm and the LTS algorithm for systems of reaction-diffusion equations. For sake of completeness, we provide versions of these algorithms adapted to the bidomain model of electrocardiology in the Appendix.

6.2. Example 1. For this example, we consider the simple monodomain model (2.8) with homogeneous Neumann boundary conditions. The ionic current and membrane model is determined by the FitzHugh-Nagumo membrane kinetics (2.3), with $a = 0.16875$, $b = 1.0$, $\lambda = -100$ and $\theta = 0.25$. The computational domain is the square $\Omega = [0, 1 \text{ cm}]^2$, and the remaining parameters are $c_m = 1.0 \text{ mF/cm}^2$ and $\beta = 1.0 \text{ cm}^{-1}$. The units for v, w are mV. We consider in (2.8) $(1 + \lambda)^{-1} \mathbf{M}_i := \text{diag}(\gamma, \gamma)$ with $\gamma = 0.01$. The respective initial data for v and w are

$$v^0(x, y) = \left(1 - \frac{1}{1 + \exp(-50(x^2 + y^2)^{1/2} - 0.1)} \right) \text{ mV}, \quad w_0 = 0 \text{ mV}.$$

After 4 ms, an instantaneous stimulus is applied in $(x_0, y_0) = (0.5 \text{ cm}, 0.5 \text{ cm})$ to the membrane potential v

$$\frac{\lambda}{1 + \lambda} I_{\text{app}} := \begin{cases} 1 \text{ mV} & \text{if } (x - x_0)^2 + (y - y_0)^2 < 0.04 \text{ cm}^2, \\ 0 \text{ mV} & \text{otherwise.} \end{cases}$$

In this example, we use $L = 10$ resolution levels, $\mathcal{N} = 262144$ elements in the finest level, a tolerance of $\varepsilon_R = 1 \times 10^{-3}$, and we compute normalized errors by comparison with a reference solution obtained with a fine mesh calculation with $\mathcal{N} = 1024^2 = 1048576$ control volumes. The time evolution is made using a first-order explicit Euler scheme. Plots of the numerical solution with the corresponding adaptively refined meshes at different times are shown in Figures 1 and 2.

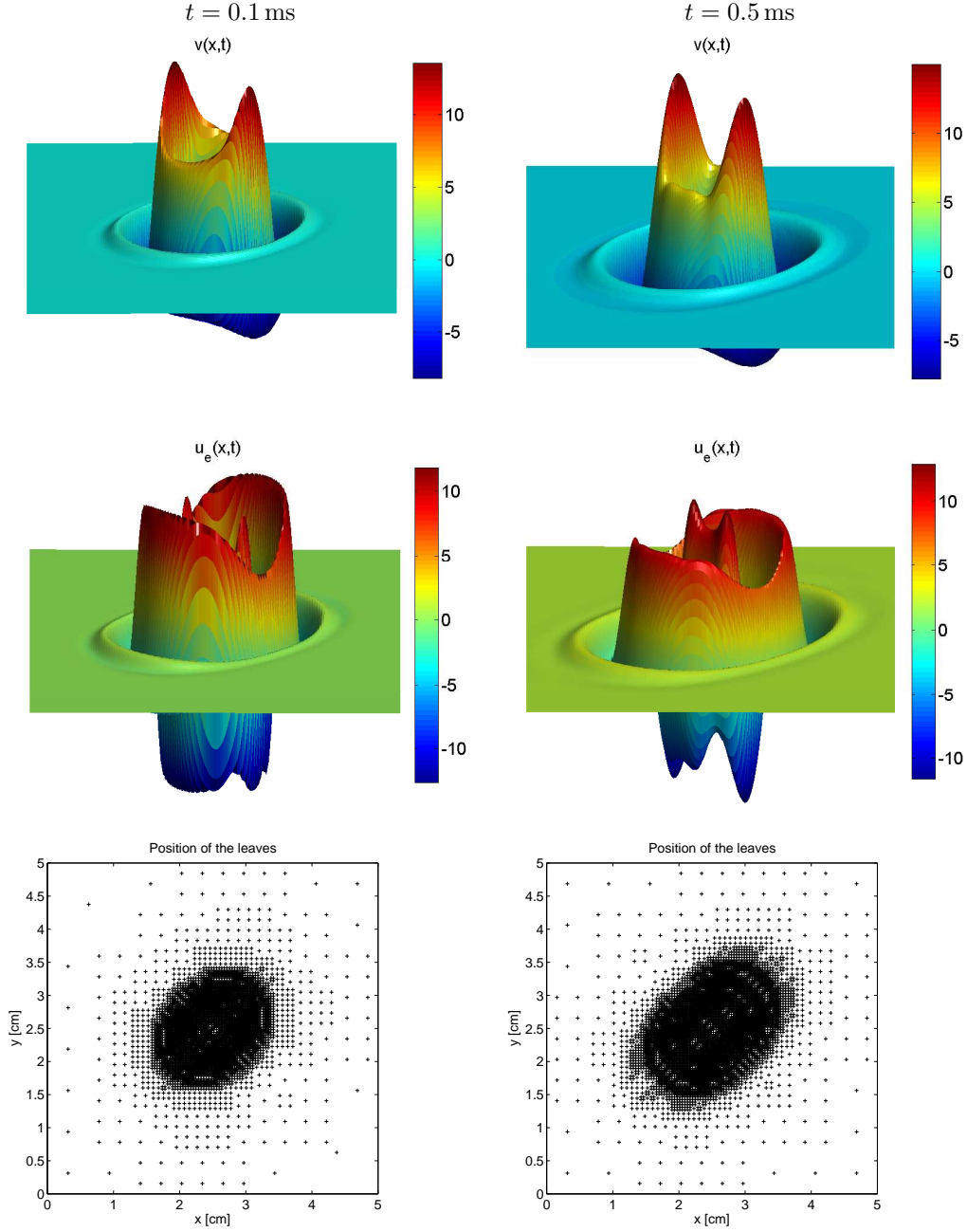


FIGURE 4. Example 2 (bidomain model, one stimulus): Numerical solution for transmembrane potential v and extracellular potential u_e in [mV], and leaves of the corresponding tree data structure at times $t = 0.1$ ms and $t = 0.5$ ms.

As can be seen from Table 1, the normalized errors are controlled to be of the same order of the reference tolerance ε_R . We also see that the MR algorithm is efficient: we have high rates of memory compression and speed-up.

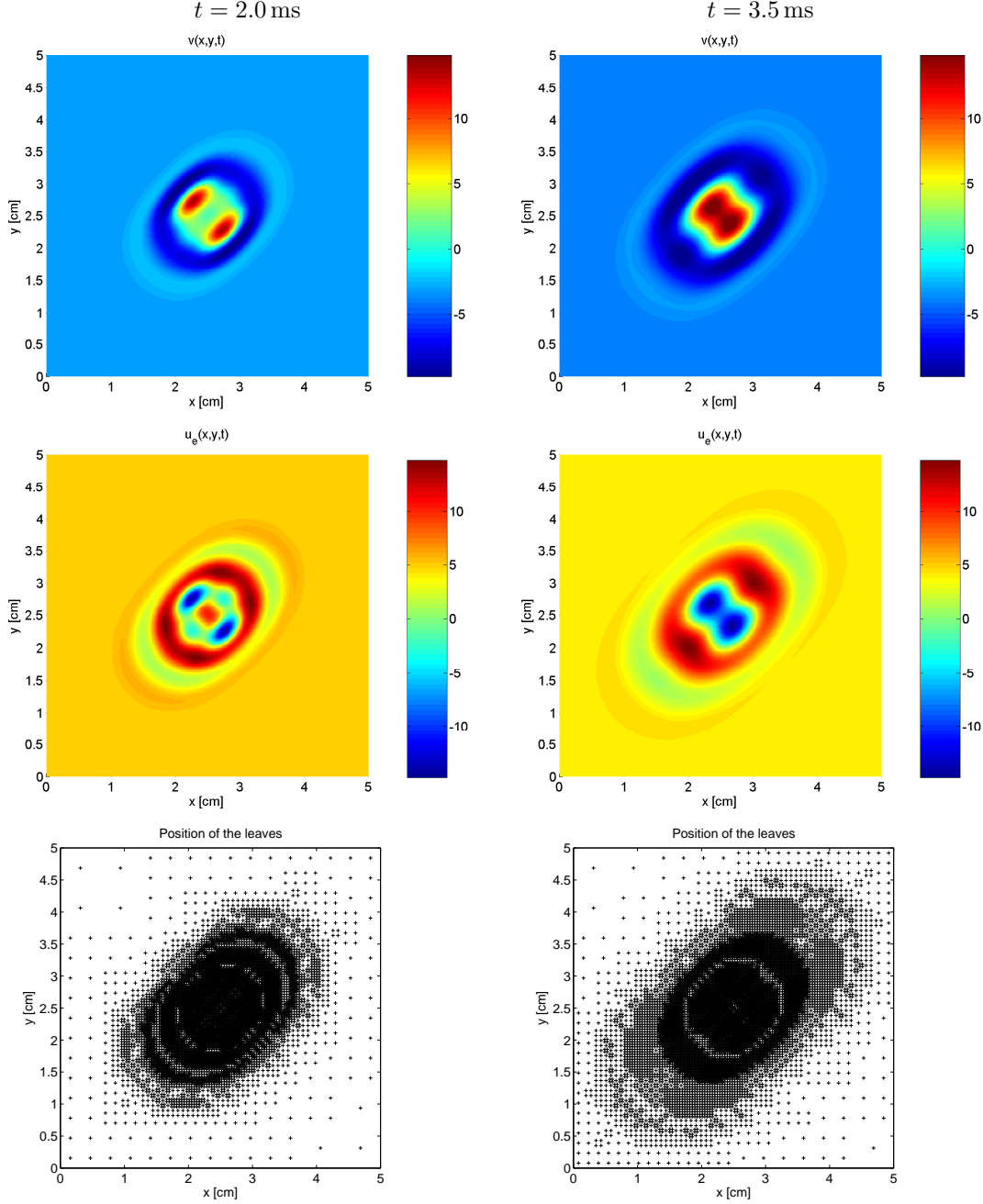


FIGURE 5. Example 2 (bidomain model, one stimulus): Numerical solution for transmembrane potential v and extracellular potential u_e in [mV], and leaves of the corresponding tree data structure at times $t = 2.0$ ms and $t = 3.5$ ms.

6.3. Example 2. In Examples 2 and 3, we present computational results for the simulation of the bidomain equations. We consider a computational domain $\Omega = [0, 5 \text{ cm}]^2$, and the parameters in (2.2) and (2.4) (after [22, 39, 43, 44]) are given by the membrane capacitance $c_m = 1.0 \text{ mF/cm}^2$, the intracellular conductivity in the principal axis $\sigma_i^1 = 6 \Omega^{-1} \text{ cm}^{-1}$, the remaining intracellular conductivity $\sigma_i^t = 0.6 \Omega^{-1} \text{ cm}^{-1}$ (corresponding

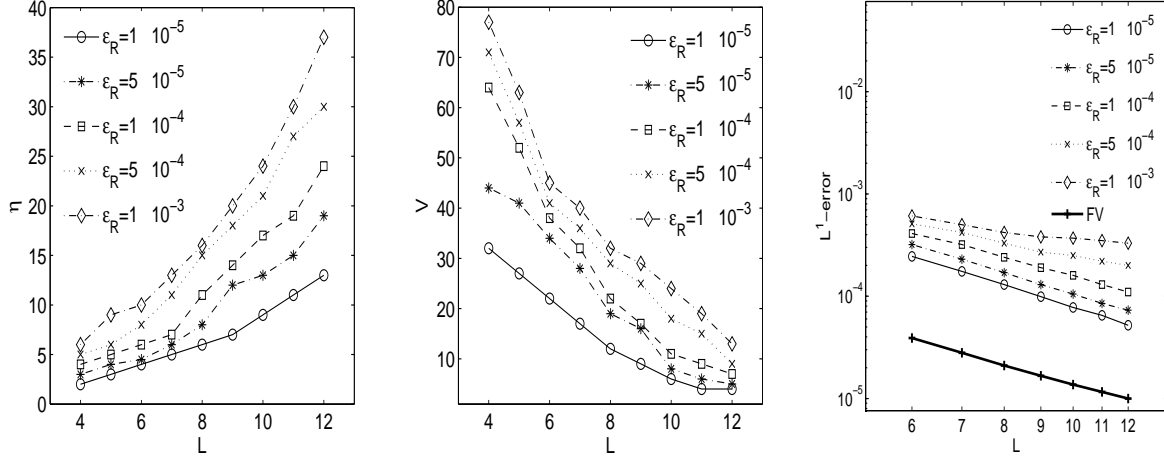


FIGURE 6. Example 2 (bidomain model): data compression rate η (left), speed-up factor \mathcal{V} (middle) and L^1 -errors for different scales L and values of ε_R (right). The simulated time is $t = 2.0$ ms.

to an anisotropy ratio of 10), the extracellular conductivities $\sigma_e^1 = 24 \Omega^{-1} \text{cm}^{-1}$ and $\sigma_e^t = 12 \Omega^{-1} \text{cm}^{-1}$ (corresponding to an anisotropy ratio of 2), the surface-to-volume ratio $\beta = 2000 \text{cm}^{-1}$, the surface resistivity $R_m = 2 \times 10^4 \Omega \text{cm}^2$, $v_p = 100 \text{mV}$, $\eta_1 = 0.005$, $\eta_2 = 0.1$, $\eta_3 = 1.5$, $\eta_4 = 7.5$, and $\eta_5 = 0.1$. The fibers form an angle of $\pi/4$ with the x -axis.

In Example 2, the initial datum is given by a stimulus applied on the extracellular potential u_e in the center of the domain, while both v and the gating variable w are initially set to zero (see Figure 3). The units for v, u_e and w are mV. In this example, the following MR setting is chosen. We utilize wavelets with $r = 3$ vanishing moments, a maximal resolution level $L = 9$, and therefore a finest mesh with $\mathcal{N} = 65536$ elements. The reference tolerance given by $\varepsilon_R = 5.0 \times 10^{-4}$.

We show in Figures 4 and 5 a sequence of snapshots after an initial stimulus applied to the center of the domain, corresponding to transmembrane potential v , extracellular potential u_e and adaptive mesh.

Table 2 illustrates the efficiency and accuracy of the base MR method by tabulating CPU ratio \mathcal{V} , compression rate η and normalized errors. By using MR, we obtain an average data compression rate of 17 and an increasing speed-up rate up to 26.09. Moreover, the errors in three different norms remain of the order of ε_R . Here we have computed normalized errors using a reference FV solution on a grid with $\mathcal{N} = 1024^2 = 1048576$ control volumes.

For the time integration using the LTS method, we choose the maximum CFL number allowed by (3.8), $\text{CFL}_{l=0} = 0.5$ for the coarsest level and $\text{CFL}_l = 2^l \text{CFL}_{l=0}$ for finer levels. For the RKF computations, we use $\delta_{\text{desired}} = 1 \times 10^{-4}$, $\mathcal{S}_0 = 0.1$, $\mathcal{S}_{\min} = 0.01$, and the initial CFL condition $\text{CFL}_{t=0} = 0.5$.

We select this example for a detailed comparison of the performance of the FV and MR methods with a global time step, the MR method with RKF adaptive global time stepping (MR-RKF), and the MR method with local time stepping (MR-LTS). The evolution of the speed-up factor \mathcal{V} and data compression rate η for the MR versions and of the normalized L^1 and L^∞ errors for all these methods are displayed in Figure 7. From these plots it is observed that with RKF and LTS, the data compression rate is of the same order during the time evolution, which means that the adaptive meshes for both methods should be roughly the same. Also, a substantial additional gain is obtained in speed-up rate when comparing with a MR calculation using global time stepping: The MR-LTS method gives us an additional speed-up factor of about 2, while with the RKF alternative we obtain an additional speed-up of about 4. This effect could be explained in part from the lack of need of a synchronization procedure for the RKF computations, and the fact that the CFL condition (3.8) is not imposed during the time evolution with the MR-RKF method, allowing larger time

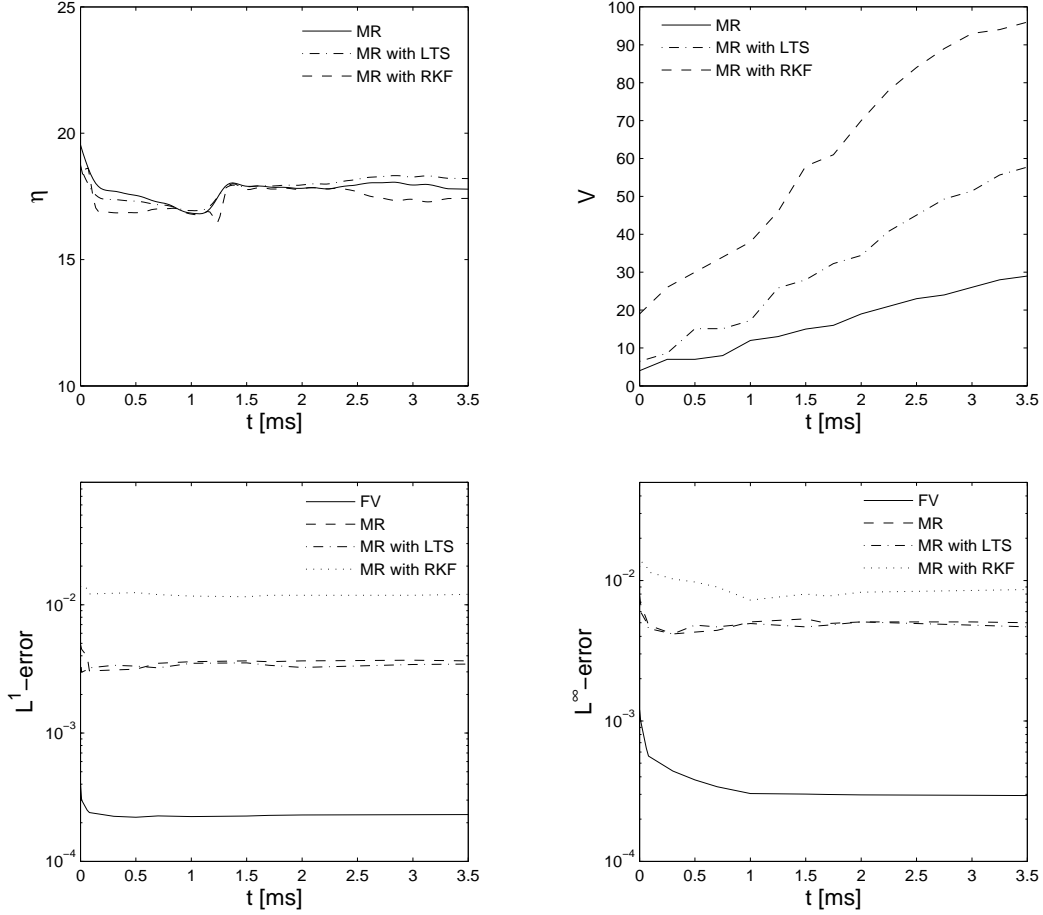


FIGURE 7. Example 2 (bidomain model, one stimulus): Time evolution for data compression rate η , speed-up rate V , and normalized errors for different methods: MR scheme with global time step, MR with locally varying time stepping and MR with RKF time stepping.

steps. (Although condition (3.8) guarantees numerical stability of the solutions, in practice this is observed to be a fairly conservative estimates, and moderately larger time steps may be used.) We can also conclude that the errors of the MR-LTS computations are kept of the same order that the errors obtained with a global time stepping, while the incurred errors by using the MR-RKF method are larger during the whole time evolution.

6.4. Example 3. For this example, we consider an initial stimulus at the center of the domain, later at $t = 0.2$ ms we apply another instantaneous stimulus to the northwest corner of the domain, and then at $t = 1.0$ ms we apply a third stimulus of the same magnitude to the northeast and southwest corners. The system is evolved and we show snapshots of the numerical solution for v, u_e and the adaptive mesh. We use the MR-RKF method with $\mathcal{N} = 65536$, $\varepsilon_R = 2.5 \times 10^{-3}$, $\delta_{\text{desired}} = 1 \times 10^{-3}$ and the remaining parameters are considered as in Example 2. As in Example 2, from Figures 8 and 9 we clearly notice the anisotropic orientation of the fibers.

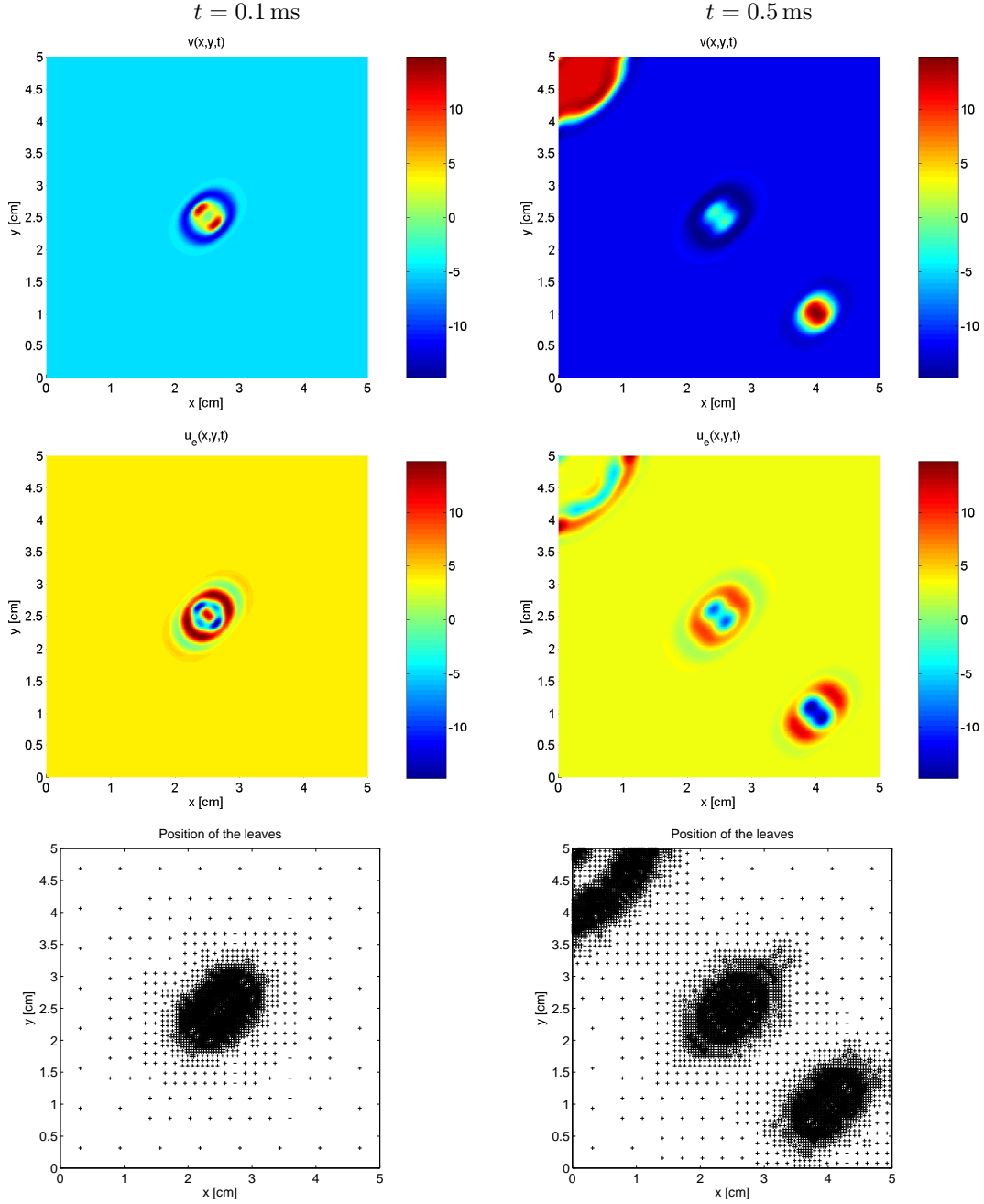


FIGURE 8. Example 3 (bidomain model, three stimuli): Numerical solution for transmembrane potential v and extracellular potential u_e in [mV], and leaves of the corresponding tree data structure at times $t = 0.1$ ms and $t = 0.5$ ms.

7. CONCLUSIONS

We address the application of a MR method for FV schemes combined with LTS and RKF adaptive time stepping for solving the bidomain equations. The numerical experiments illustrate that these methods are efficient and accurate enough to simulate the electrical activity in myocardial tissue with affordable effort.

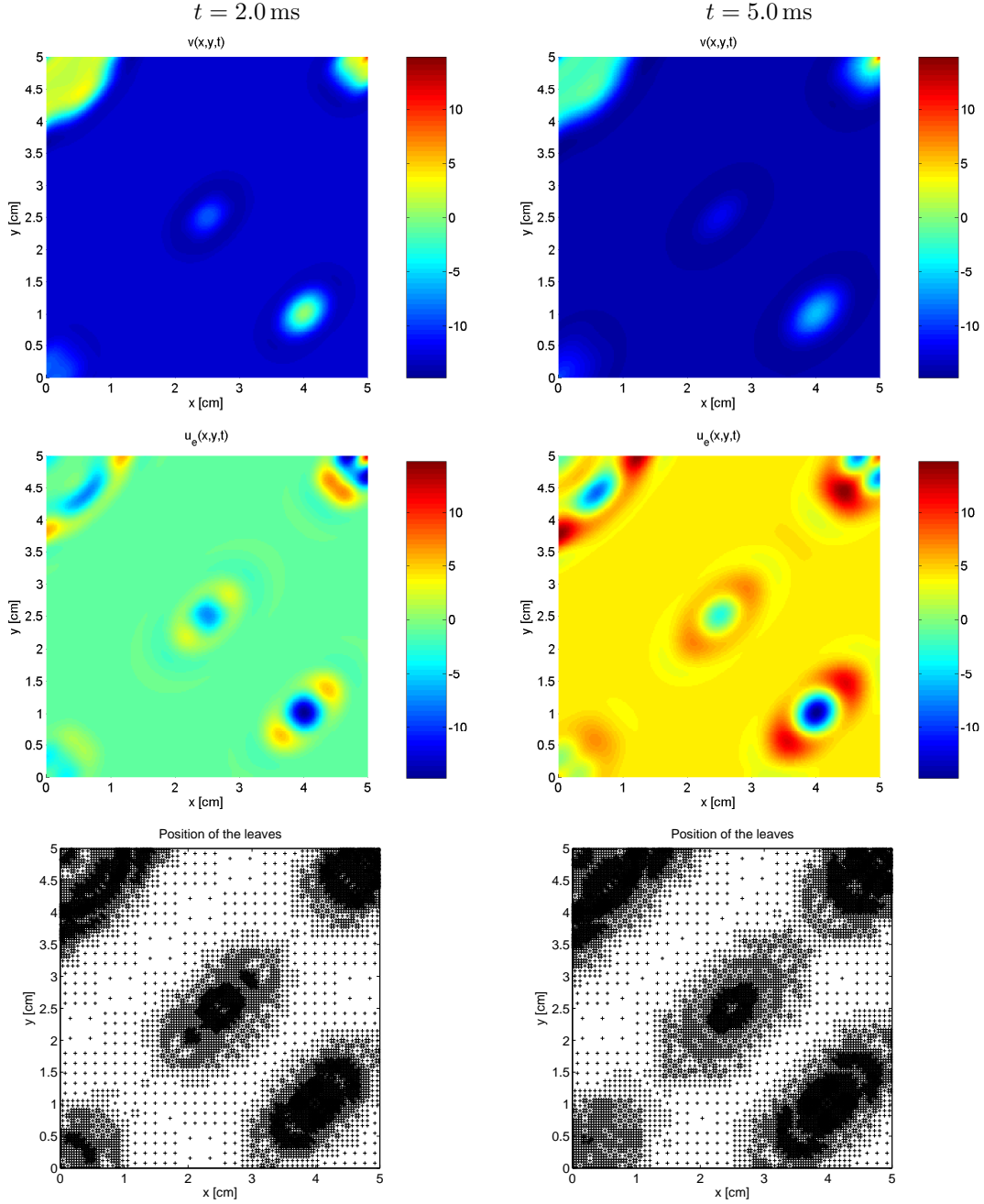


FIGURE 9. Example 3 (bidomain model, three stimuli): Numerical solution for transmembrane potential v and extracellular potential u_e in [mV], and leaves of the corresponding tree data structure at times $t = 2.0$ ms and $t = 5.0$ ms.

This is a real advantage in comparison with more involved methods that require large scale computations on clusters. We here contribute to the recent work done by several groups in testing whether the combination of MR, LTS and RKF strategies is indeed effective for a relevant class of problems.

From a numerical point of view, the plateau-like structures, associated with very steep gradients, of typical solutions motivate the use of a locally refined adaptive mesh, since we require high resolution near these steep gradients only. These areas of strong variation occupy a very reduced part of the entire domain only, especially in the case of sharp fronts. Consequently our gain will be less significant in the presence of chaotic electrical activity or when multiple waves interact in the considered tissue.

Based on our numerical examples, we conclude that using a LTS strategy, we obtain a substantial gain in CPU time speed-up for a factor of about 2 for larger scales while the errors between the MR-LTS solution and a reference solution are of the same order as those of the MR solution. On the other hand, using an MR-RKF strategy, we obtain an additional speed-up factor of about 4, but at the price of larger errors. However, in assessing our findings, it is important to recognize limitations. The high rates of compression obtained with our methods are problem-dependent and they may depend on the proper adjustment of parameters. We have only considered here very simple geometries, because all computations are concentrated on adaptivity and performance. Simulations on more complex and realistic geometries are part of possible future work.

Finally, we remark that the FV method given in Section 3 as well the MR framework detailed in Section 4 are both straightforwardly extensible to the 3D case. A convergence analysis of the implicit version of the FV method presented in Section 3 is being prepared [1].

ACKNOWLEDGEMENTS

MB acknowledges support by Fondecyt project 1070682, RB acknowledges support by Fondecyt project 1050728 and Fondap in Applied Mathematics, project 15000001 and RR acknowledges support by Conicyt Fellowship and Mecusup project UCO0406.

APPENDIX

For illustrative purposes, suppose that we are in the case of a cartesian mesh. We give here an example of an interior first-order flux calculation using LTS for the parabolic part of the bidomain scheme (the equation for v), needed to complete a full macro time step, by the following algorithm:

Algorithm 2 (Locally varying intermediate time stepping).

- (1) *Grid adaptation (provided the former sets of leaves).*
- (2) **do** $k = 1, \dots, 2^L$ (for the local time steps $n + 2^{-L}, n + 2 \cdot 2^{-L}, n + 3 \cdot 2^{-L}, \dots, n + 1$)
 - (a) *Synchronization:*
 - do** $l = L, \dots, 1$
 - do** $i = 1, \dots, |\tilde{\Lambda}|_x(l), j = 1, \dots, |\tilde{\Lambda}|_y(l)$
 - if** $1 \leq l \leq \tilde{l}_{k-1}$ **then**
 - if** $V_{(i,j),l}$ is a virtual leaf **then**

$$\bar{F}_{(i,j),l \rightarrow (i+1,j),l}^{n+k2^{-L}} \leftarrow \bar{F}_{(i,j),l \rightarrow (i+1,j),l}^{n+(k-1)2^{-L}}$$

$$\text{Update reaction terms:}$$

$$I_{\text{ion}(i,j),l}^{n+k2^{-L}} \leftarrow I_{\text{ion}(i,j),l}^{n+(k-1)2^{-L}}, \quad I_{\text{app}(i,j),l}^{n+k2^{-L}} \leftarrow I_{\text{app}(i,j),l}^{n+(k-1)2^{-L}}$$
 - endif**
 - else**
 - if** $V_{(i,j),l}$ is a leaf **then**

$$I_{\text{ion}(i,j),l}^{n+k2^{-L}} \leftarrow I_{\text{ion}}(v_{(i,j),l}^{n+k2^{-L}}, w_{(i,j),l}^{n+k2^{-L}}),$$

$$I_{\text{app}(i,j),l}^{n+k2^{-L}} \leftarrow I_{\text{app}}(v_{(i,j),l}^{n+k2^{-L}}, w_{(i,j),l}^{n+k2^{-L}})$$
 - if** $V_{(i+1,j),l}$ is a leaf **then**

$$\bar{F}_{(i,j),l \rightarrow (i+1,j),l} \leftarrow -\frac{d_e^*}{h(l)} \frac{|\sigma_{V_{(i,j),l}, V_{(i+1,j),l}}|}{d(V_{(i,j),l}, V_{(i+1,j),l})} (u_{e,(i+1,j),l} - u_{e,(i,j),l})$$

```


$$\bar{F}_{(i,j),l \rightarrow (i,j+1),l} \leftarrow -\frac{d_e^*}{h(l)} \frac{|\sigma_{V_{(i,j),l}, V_{(i,j+1),l}}|}{d(V_{(i,j),l}, V_{(i,j+1),l})} (u_{e,(i,j+1),l} - u_{e,(i,j),l})$$

endif
if  $V_{(2i+2,2j),l+1}, V_{(2i+2,2j+1),l+1}$  are leaves (interface edges) then

$$\bar{F}_{(i,j),l \rightarrow (i+1,j),l} \leftarrow \bar{F}_{2(i+1,j),l+1 \rightarrow (2i+1,2j),l+1} + \bar{F}_{(2i+2,2j+1),l+1 \rightarrow (2i+1,2j+1),l+1}$$


$$\bar{F}_{(i,j),l \rightarrow (i,j+1),l} \leftarrow \bar{F}_{2(i,j+1),l+1 \rightarrow (2i,2j+1),l+1} + \bar{F}_{(2i+1,2j+2),l+1 \rightarrow (2i+1,2j+1),l+1}$$

endif
endif
endif
enddo
enddo
(b) Time evolution:
do  $l = 1, \dots, L, i = 1, \dots, |\tilde{\Lambda}|_x(l), j = 1, \dots, |\tilde{\Lambda}|_y(l)$ 
if  $1 \leq l \leq \tilde{l}_{k-1}$  then there is no evolution:

$$v_{(i,j),l}^{n+(k+1)2^{-L}} \leftarrow v_{(i,j),l}^{n+k2^{-L}}$$

else
Marching formula only for the leaves  $V_{(i,j),l}$ :

$$v_{(i,j),l}^{n+(k+1)2^{-L}} \leftarrow \frac{1}{c_m} v_{(i,j),l}^{n+k2^{-L}} + \frac{\Delta t_l}{c_m} I_{\text{app}(i,j),l}^{n+k2^{-L}} - \frac{\Delta t_l}{c_m} I_{\text{ion}(i,j),l}^{n+k2^{-L}}$$


$$- \frac{\Delta t_l}{c_m} \sum_{(n,m) \in \mathcal{S}((i,j),l)} \frac{d_e^*}{h(l)} \frac{|\sigma_{V_{(i,j),l}, V_{(n,m),l}}|}{d(V_{(i,j),l}, V_{(n,m),l})} (u_{e,(n,m),l} - u_{e,(i,j),l})$$

endif
enddo
(c) Partial grid adaptation each odd intermediate time step:
do  $l = L, \dots, \tilde{l}_k + 1$ 
Projection from the leaves.
enddo
do  $l = \tilde{l}_k, \dots, L$ 
Thresholding, prediction, and addition of the safety zone.
enddo
enddo

```

Here, \tilde{l}_k denotes the coarsest level containing leaves in the intermediate step k , $h(l)$ is the mesh size on level l , and $|\tilde{\Lambda}|_z(l)$ is the size of the set formed by leaves and virtual leaves per resolution level l in the direction z . The marching formula corresponds to (3.4), for the intermediate time steps $k = 1, \dots, 2^L$, for the leaf $V_{(i,j),l}$.

Now we give a brief description of the general multiresolution procedure.

Algorithm 3 (Multiresolution procedure).

- (1) *Initialization of parameters.*
- (2) *Creation of the initial tree:*
 - (a) *Create the root and compute its cell average value.*
 - (b) *Split the cell, compute the cell average values in the sons and compute details.*
 - (c) *Apply thresholding for the splitting of the new sons.*
 - (d) *Repeat this until all sons have details below the required tolerance ε_l .*
- (3) **do** $n = 1, \dots, \text{total_time_steps}$
 - (a) *Determination of the leaves and virtual leaves sets.*
 - (b) *Time evolution with global time step: Compute the discretized space operator \mathcal{A} for all the leaves.*
 - (c) *Updating the tree structure:*

- Recalculate the values on the nodes by projection from the leaves. Compute the details for all positions (\cdot, \cdot, l) for $l \geq \tilde{l}_k$. If the detail in a node and in its brothers is smaller than the prescribed tolerance, then the cell and its brothers are deletable.
- If some node and all its sons are deletable, and the sons are leaves without virtual sons, then delete sons. If this node has no sons and it is not deletable and it is not at level $l = L$, then create sons.
- Update the values in the new sons by prediction from the former leaves.

enddo

(4) *Output: Save meshes, leaves and cell averages.*

Here $total_time_steps$ is the total time steps needed to reach T_{final} using Δt as the maximum time step allowed by the CFL condition using the finest space step.

When using a RKF strategy for the time evolution, replace step (3b) by the new step

- (3) • Compute the discretized space operator \mathcal{A} for all the leaves as in (5.1).
 • Compute the difference between the two solutions obtained as in (5.2).
 • Apply the limiter for the time step variation and compute the new time step by (5.3).

When using a LTS strategy, replace step (3b) by the new step

- (3) **do** $n = 1, \dots, total_time_steps$
 (a) *Determination of the leaves and virtual leaves sets.*
 (b) *Time evolution with local time stepping: Compute the discretized space operator \mathcal{A} for all the leaves and virtual leaves*
 (c) **do** $k = 1, \dots, 2^L$ (k counts intermediate time steps)
 • Compute the intermediate time steps depending on the position of the leaf as explained in Section 5.1.
 • **if** k is odd **then** update the tree structure:
 – Recalculate the values on the nodes and the virtual nodes by projection from the leaves. Compute the details in the whole tree. If the detail in a node is smaller than the prescribed tolerance, then the cell and its brothers are deletable.
 – If some node and all its sons are deletable, and the sons are leaves without virtual sons, then delete sons. If this node has no sons and it is not deletable and it is not at level $l = L$, then create sons.
 – Update the values in the new sons by prediction from the former leaves.

endif

enddo

(Now, after 2^L intermediate steps, all the elements are synchronized.)

enddo

Here $total_time_steps$ is the total time steps needed to reach T_{final} , with Δt_0 as the maximum time step allowed by the CFL condition using the coarsest space step.

REFERENCES

- [1] M. Bendahmane, R. Bürger, R. Ruiz, Convergence of a finite volume scheme for the bidomain model of electrocardiology, in preparation.
- [2] M. Bendahmane, R. Bürger, R. Ruiz, K. Schneider, Adaptive multiresolution schemes with local time stepping for two-dimensional degenerate reaction-diffusion systems. Preprint 2007-35, Depto. Ing. Mat., U. de Concepción, available from <http://www.ing-mat.udec.cl/>; submitted.
- [3] M. Bendahmane, K.H. Karlsen, Analysis of a class of degenerate reaction-diffusion systems and the bidomain model of cardiac tissue, *Netw. Heterog. Media* 1 (2006) 185–218.
- [4] M. Bendahmane, K.H. Karlsen, Convergence of a finite volume scheme for the bidomain model of cardiac tissue, Preprint 2007-24, Depto. Ing. Mat., U. de Concepción, available from <http://www.ing-mat.udec.cl/>; submitted.
- [5] M.J. Berger, J. Olinger, Adaptive mesh refinement for hyperbolic partial differential equations, *J. Comput. Phys.* 53 (1984) 482–512.
- [6] Y. Bourgault, Y. Coudière, C. Pierre, Existence and uniqueness of the solution for the bidomain model used in cardiac electro-physiology, *Nonlin. Anal. Real World Appl.*, to appear.

- [7] R. Bürger, A. Kozakevicius, M. Sepúlveda, Multiresolution schemes for degenerate parabolic equations in one space dimension, *Numer. Meth. Partial Diff. Eqns.* 23 (2007) 706–730.
- [8] R. Bürger, R. Ruiz, K. Schneider, M. Sepúlveda, Fully adaptive multiresolution schemes for strongly degenerate parabolic equations in one space dimension, *M2AN Math. Model. Numer. Anal.*, to appear.
- [9] R. Bürger, R. Ruiz, K. Schneider, M. Sepúlveda, Fully adaptive multiresolution schemes for strongly degenerate parabolic equations with discontinuous flux, *J. Engrg. Math.* 60 (2008) 365–385.
- [10] H. Chen, X.-H. Zhong, Global existence and blow-up for the solutions to nonlinear parabolic/elliptic system modelling chemotaxis, *IMA J. Appl. Math.* 70 (2005) 221–240.
- [11] E. Cherry, H. Greenside, C.S. Henriquez, Efficient simulation of three-dimensional anisotropic cardiac tissue using an adaptive mesh refinement method, *Chaos* 13 (2003) 853–865.
- [12] G. Chiavassa, R. Donat, S. Müller, Multiresolution-based adaptive schemes for hyperbolic conservation, in: T. Plewa, T. Linde, V.G. Weiss (Eds.), *Adaptive Mesh Refinement-Theory and Applications*, Springer-Verlag, Berlin, 2003, pp. 137–159.
- [13] A. Cohen, S. Kaber, S. Müller, M. Postel, Fully adaptive multiresolution finite volume schemes for conservation laws, *Math. Comp.* 72 (2001) 183–225.
- [14] P. Colli Franzone, P. Deuffhard, B. Erdmann, J. Lang, L.F. Pavarino, Adaptivity in space and time for reaction–diffusion systems in electro-cardiology, *SIAM J. Sci. Comput.* 28 (2006) 942–962.
- [15] P. Colli Franzone, L.F. Pavarino, A parallel solver for reaction-diffusion systems in computational electro-cardiology, *Math. Models Meth. Appl. Sci.* 14 (2004) 883–911.
- [16] P. Colli Franzone, L.F. Pavarino, B. Taccardi, Simulating patterns of excitation, repolarization and action potential duration with cardiac Bidomain and Monodomain models, *Math. Biosci.*, 197 (2005), 35–66.
- [17] P. Colli Franzone, G. Savaré, Degenerate evolution systems modeling the cardiac electric field at micro- and macroscopic level, in: A. Lorenzi, B. Ruf (Eds.), *Evolution equations, semigroups and functional analysis*, Birkhäuser, Basel, 2002, pp. 49–78.
- [18] Y. Coudière, C. Pierre, R. Turpault, Solving the fully coupled heart and torso problems of electro cardiology with a 3D discrete duality finite volume method, *HAL preprint* (2006), available from <http://hal.archives-ouvertes.fr/ccsd-00016825>.
- [19] W. Dahmen, B. Gottschlich-Müller, S. Müller, Multiresolution schemes for conservation laws, *Numer. Math.* 88 (2001) 399–443.
- [20] M. Domingues, O. Roussel, K. Schneider, An adaptive multiresolution method for parabolic PDEs with time step control, *ESAIM: Proc.* 16 (2007) 181–194.
- [21] M. Domingues, S. Gomes, O. Roussel, K. Schneider, An adaptive multiresolution scheme with local time-stepping for evolutionary PDEs, *J. Comput. Phys.* 227 (2008) 3758–3780.
- [22] E. Entcheva, J. Eason, F. Claydon, R. Malkin, Spatial effects from bipolar current injection in 3D myocardium: implications for conductivity measurements, *Computers in Cardiology* 7 (1997) 717–720.
- [23] R. Eymard, T. Gallouët, R. Herbin, Finite volume methods, in P.G. Ciarlet, J.L. Lions (Eds.), *Handbook of Numerical Analysis*, vol. VII, North-Holland, Amsterdam, 2000, pp. 713–1020.
- [24] E. Fehlberg, Low order classical Runge-Kutta formulas with step size control and their application to some heat transfer problems, *Computing* 6 (1970) 61–71.
- [25] R. FitzHugh, Impulses and physiological states in theoretical models of nerve membrane, *Biophys. J.* 1 (1961) 445–465.
- [26] A. Harten, Multiresolution algorithms for the numerical solution of hyperbolic conservation laws, *Comm. Pure Appl. Math.* 48 (1995) 1305–1342.
- [27] A.L. Hodgkin, A.F. Huxley, A quantitative description of membrane current and its application to conduction and excitation in nerve, *J. Physiol.* 117 (1952) 500–544.
- [28] J. Keener, J. Sneyd, *Mathematical Physiology*, Corr. Second Printing, Springer-Verlag, New York, 2001.
- [29] C. Mitchell, D. Schaeffer, A two-current model for the dynamic of cardiac membrane, *Bull. Math. Biol.* 65 (2001) 767–793.
- [30] S. Müller, *Adaptive Multiscale Schemes for Conservation Laws*, Springer-Verlag, Berlin, 2003.
- [31] S. Müller, Y. Stiriba, Fully adaptive multiscale schemes for conservation laws employing locally varying time stepping, *J. Sci. Comput.* 30 (2007) 493–531.
- [32] J.S. Nagumo, S. Arimoto, S. Yoshizawa, An active pulse transmission line simulating nerve axon, *Proc. Inst. Radio Eng.* 50 (1962) 2061–2071.
- [33] D. Noble, A modification of the Hodgkin-Huxley equations applicable to Purkinje fibre action and pacemaker potentials, *J. Physiol.* 160 (1962) 317–352.
- [34] M. Pennacchio, V. Simoncini, Efficient algebraic solution of reactiondiffusion systems for the cardiac excitation process, *J. Comp. App. Math.* 145-1 (2002) 49–70.
- [35] W. Quan, S. Evans, H. Hastings, Efficient integration of a realistic two-dimensional cardiac tissue model by domain decomposition, *IEEE Trans. Biomed. Eng.* 45 (1998) 372–385.
- [36] O. Roussel, K. Schneider, An adaptive multiresolution method for combustion problems: application to flame ball-vortex interaction, *Computers & Fluids* 34 (2005) 817–831.
- [37] O. Roussel, K. Schneider, A. Tsigulin, H. Bockhorn, A conservative fully adaptive multiresolution algorithm for parabolic PDEs, *J. Comput. Phys.* 188 (2003) 493–523.

- [38] H. Saleheen, K. Ng, A new three-dimensional finite-difference bidomain formulation for inhomogeneous anisotropic cardiac tissues, *IEEE Trans. Biomed. Eng.* 45 (1998) 15–25.
- [39] K. Skouibine, N. Trayanova, P. Moore, A numerically efficient model for simulation of defibrillation in an active bidomain sheet of myocardium, *Math. Biosci.* 166 (2000) 85–100.
- [40] J. Sundnes, G.T. Lines, X. Cai, B.F. Nielsen, K.-A. Mardal, A. Tveito, *Computing the Electrical Activity in the Heart*, Springer-Verlag, Berlin, 2006.
- [41] J. Trangenstein, C. Kim, Operator splitting and adaptive mesh refinement for the Luo-Rudy I model, *J. Comput. Phys.* 196 (2004) 645–679.
- [42] L. Tung, *A Bi-Domain Model for Describing Ischemic Myocardial D-C Currents*, PhD thesis, MIT, Cambridge, MA, 1978.
- [43] W.-J. Ying, *A Multilevel Adaptive Approach for Computational Cardiology*, PhD Thesis, Department of Mathematics, Duke University, 2005.
- [44] W.-J. Ying, D.J. Rose, C.S. Henriquez, *Efficient fully implicit time integration methods for modeling cardiac dynamics*, Technical Report, Duke University, 2007.